Journal of Alloys and Compounds 1065 (2026) 188279

Contents lists available at ScienceDirect

Journal of Alloys and Compounds

journal homepage: www.elsevier.com/locate/jalcom

Role of ZnO morphology in promoting NiO heterojunction formation and enhanced gas sensing

P.P. Ortega [a,*], S. Gherardi [b,c], E. Spagnoli [d], G. Zonta [b,c], M. Astolfi [b,c], G. Cruciani [c], V.R. Mastelaro [e], M.A. Ponce [f], C. Malagù [c], E. Longo [a]

[a] Center for the Development of Functional Materials (CDMF), Federal University of São Carlos (UFSCar), São Carlos, São Paulo 13565-905, Brazil
[b] SCENT S.r.l., Via Quadrifoglio 11, Ferrara 44124, Italy
[c] University of Ferrara (UNIFE), Department of Physics and Earth Sciences, Via Saragat 1, Ferrara 44122, Italy
[d] Institute of nanostructured materials (ISMN), CNR, Via P. Gobetti 101, Bologna 40129, Italy
[e] São Carlos Institute of Physics (IFSC), University of São Paulo (USP), São Carlos 13566-590, Brazil
[f] Physics and Engineering Research Center CIFICEN (UNCPBA-CICPBA-CONICET), Tandil B7000GHG, Argentina

ARTICLE INFO

Keywords:
Morphology
Heterojunction
Zinc oxide
Gas sensor

ABSTRACT

Zinc oxide samples with plate and rod morphologies were synthesized via the microwave-assisted hydrothermal (MAH) method and decorated with NiO to form heterostructures. Rietveld refinement revealed NiO contents of ~25 wt% and ~40 wt% for each morphology. The ZnO plates demonstrated superior response to 1 ppm ethanol compared to ZnO rods, attributed to their more reactive exposed crystal facets and stronger depletion layer effects. Upon decoration with 25 wt% NiO (ZnO-P-20Ni), the ethanol response increased by 275% and 410% relative to the pure ZnO plates and rods, respectively. Conductance measurements confirmed the p–n heterojunction formation only in ZnO-P-20Ni, with conductance decreasing from 1.7×10^{-7} to 7.6×10^{-8} S at 350°C compared to the ZnO plates. In contrast, 40 wt% NiO and all rod-based heterostructures showed no improvements, likely due to parallel conduction through NiO. The plate-like ZnO/NiO heterostructures displayed improved sensing properties across all testing conditions in dry air and better performance for CO sensing under humid conditions. The plates retained 75% of the ethanol response under 40% relative humidity. These findings highlight the importance of ZnO morphology in enhancing gas sensing performance and enabling heterojunction formation, providing a valuable strategy for designing efficient chemoresistive sensors.

1. Introduction

Metal oxide semiconductors (MOSs) have long been recognized as exceptional materials for gas sensing applications. Their chemoresistive sensing mechanism offers several advantages, including high sensitivity, low cost, simple fabrication, and scalability [1–3]. However, achieving high selectivity and stability remains a challenge. The primary limitation arises from the non-specific nature of the sensing signal, which is based on changes in conductance upon interaction with different gaseous species. This often leads to cross-sensitivity, in which the sensor responds to multiple gases simultaneously, making it difficult to distinguish the target gas from a mixture [4–7]. One of the most critical challenges arising from cross-sensitivity is humidity-induced interference [7–9]. Water vapor, a ubiquitous atmospheric component, competes with target gases for reactive sites, ultimately reducing sensing accuracy. For instance, Nasriddinov *et al.* [10] showed that humidity significantly affects the NH_3-sensing properties of In_2O_3 and In_2O_3/rGO. They observed that for pure In_2O_3, no response was detected under high-humidity conditions, whereas for In_2O_3/rGO composites, the response signal inverted, a phenomenon attributed to the formation of new species resulting from the interaction of NH_3 with water molecules. In another work, Perfecto *et al.* [11] studied the humidity interference on the properties of ZnO and NiS/ZnO hollow spheres. The authors found that humidity significantly affected the ZnO sensitivity to butanone, reducing the response by over 90% from 0% to 25% relative humidity. While NiS/ZnO exhibited a lower response than pure ZnO, it achieved better humidity resistance.

A key advantage of using MOSs is their versatility, which can be tailored to specific purposes. In this regard, many studies show improved results across diverse applications, including doping,

* Corresponding author.
E-mail address: pedro.ortega@ufscar.br (P.P. Ortega).

https://doi.org/10.1016/j.jallcom.2026.188279
Received 31 January 2026; Received in revised form 15 April 2026; Accepted 26 April 2026
Available online 27 April 2026
0925-8388/© 2026 The Authors. Published by Elsevier B.V. This is an open access article under the CC BY license (http://creativecommons.org/licenses/by/4.0/).

morphological control, decoration, formation of heterostructures or a combination of these [12–16]. Additionally, recent developments have explored light-excited mechanisms to further enhance the gas-detection performance of MOSs sensors [17,18]. Within each of these categories, a myriad of possibilities arises from choices in dopant, morphology, heterojunction type, and more, offering vast research opportunities. Among these methods, morphological tuning and heterostructure formation are particularly prominent [19–22]. For instance, Wang *et al.* [23] demonstrated that tailoring the morphology of SnO_2 nanostructures to expose high-energy facets such as {111} and {221} significantly enhances their gas-sensing performance. The samples enclosed by these facets, synthesized using tetramethylammonium hydroxide (TMAH), exhibited superior chemical activity due to the higher density of unsaturated surface atoms, highlighting the critical role of morphology in tuning sensing properties. Liu *et al.* [24] synthesized NiO/ZnO hollow microspheres and demonstrated a significantly enhanced toluene sensing performance, attributed to the formation of a p-n heterojunction; however, their experiments were conducted under a relative humidity range of 18–25% without exploring its effect. Therefore, investigating the effect of morphology and heterostructure formation on gas-sensing properties is a promising topic for current and future research on gas sensors.

In this work, we synthesized sub-micron zinc oxide samples exhibiting rod and plate morphologies. Heterostructures with nickel oxide (with two different NiO wt%) were subsequently created for each ZnO morphology using the microwave-assisted hydrothermal (MAH) method. Then, thick films were prepared from these samples via screen-printing. We comprehensively investigated the gas-sensing properties, elucidating the effects of temperature, humidity, and target gas, and highlighting the roles of morphology and heterostructure formation in sensing performance.

2. Experimental section

2.1. Synthesis of the ZnO nanostructures

Zinc oxide nanostructures were synthesized using the MAH method. Analytical grade zinc acetate dihydrate ($Zn(CH_3CO_2)_2{\cdot}2H_2O$, Sigma-Aldrich) and sodium hydroxide (NaOH, Neon) were used as chemical reagents. To synthesize ZnO plates and rods, 1:5 and 1:10 molar ratios of zinc acetate dihydrate to sodium hydroxide were used, respectively. The procedure consisted of preparing the zinc acetate dihydrate (Solution 1, 0.1 M for plates and 0.05 M for rods) and sodium hydroxide (Solution 2, 0.5 M) solutions separately in 40 mL of deionized water, both at room temperature and under constant agitation using a magnetic stirrer. Then, Solution 1 was slowly added to Solution 2 and homogenized for 30 min, forming a white suspension (except for the rods, which initially appeared transparent, turning white after homogenization). Afterward, it was transferred to a PTFE autoclave and placed in a microwave-heating system. The synthesis was conducted at 130°C for 8 min, using a heating rate of 10°C per minute. The resulting product was washed several times until the pH reached 7, using a centrifuge to separate the solid and liquid phases. The samples were obtained after drying at 90°C for 12 h.

2.2. Synthesis of the NiO nanostructures

Nickel oxide nanodisks were synthesized using the MAH method. Analytical grade nickel nitrate hexahydrate ($Ni(NO_3)_2{\cdot}6H_2O$, Sigma-Aldrich) and sodium hydroxide (NaOH, Neon) were used as reagents. For the synthesis of the nanodisks, a solution of the nickel reagent was prepared by dissolving it in 80 mL of deionized water at room temperature (0.05 M). Then, a 2 M solution of sodium hydroxide was slowly added until the pH reached 11, while the solution was stirred continuously. After homogenization, the solution was transferred to a PTFE autoclave and placed in a microwave-heating oven. The synthesis was performed at 140°C for 8 min (10 °C/min heating rate). The synthesis product was washed with deionized water until pH 7. The samples were dried at 90°C for 12 h, resulting in a bright green powder. Finally, a calcination step at 400°C (heating rate of 10 °C/min) for 1 h was performed to obtain black NiO powder.

2.3. Synthesis of the ZnO/NiO heterostructures

The synthesis of the ZnO/NiO heterostructures consisted of two steps. In the first, described in Section 2.1, ZnO rods and plates were obtained. In the second step, 600 mg of each sample (rods or plates) was ground and dispersed in 80 mL of deionized water by ultrasonication for 1 h, forming a white suspension. Next, nickel nitrate hexahydrate was dissolved in the ZnO suspension, and the same procedure described in Section 2.2 was then employed to synthesize the NiO nanodisks. Two nickel nitrate hexahydrate solutions (0.05 M and 0.025 M) were combined with 600 mg of ZnO rods or plates to produce heterostructures with varying NiO percentages. To ensure uniformity in all thermal treatment parameters, the heterostructures were simultaneously heat-treated in the same muffle furnace.

2.4. Structural characterization of the pure and heterostructured samples

X-ray diffraction (XRD) patterns were acquired using a Bruker D8 Advance DaVinci diffractometer. This system employed a CuKα X-ray source and a LynxEye-XT strip detector to collect the diffracted intensities. Data were recorded over a 2θ range of 10–130°, with a step size of 0.02° and a counting time of 2 s per step, while the samples were continuously rotated. The Rietveld refinement of the XRD data was performed using the Bruker Topas software package. The structural models employed for this refinement were zincite for ZnO (space group $P6_3$ mc) and bunsenite for NiO (space group $Fm\bar{3}m$). Preferred orientation was corrected by March Dollase or Spherical Harmonics models, while Stephens model accounted for the anisotropic broadening. The volume-weighted apparent crystallite size was calculated based on a double-Voigt approach in which the Voigt-function approximation for both size-broadened and strain-broadened profiles was adopted. Field-emission scanning electron microscopy (FE-SEM) and transmission electron microscopy (TEM) were used to determine the morphology and exposed facets of the nanostructures. In addition, elemental mapping was performed using energy dispersive X-ray spectroscopy (EDS) integrated with the FE-SEM instrument. These analyses were conducted using a Zeiss Supra 35-VP (FE-SEM/EDS) and an FEI Tecnai G2 F20 (TEM). The ultraviolet-visible spectroscopy (UV-Vis) data were collected in diffuse reflectance spectroscopy (DRS) mode (and absorbance for pure NiO) using a Shimadzu UV-2600i spectrophotometer in the 200–1000 nm range (Figure S8). The obtained data were converted using the Kubelka–Munk function, and the resulting transformed data were then used to generate plots for band gap energy determination, following a similar approach to the Tauc plot analysis [25]. Mott–-Schottky curves were measured using an Autolab PGSTAT 204 workstation (three-electrode cell: Pt wire counter, Ag/AgCl reference) to determine the flat-band potential of the samples (via drop-cast on 1 cm^2 FTO) in 0.5 M Na_2SO_4. A Scienta Omicron ESCA spectrometer (monochromatic Al-Kα source) was employed for the X-ray photoelectron spectroscopy (XPS) characterization. The resulting data were calibrated to the adventitious carbon component at 284.8 eV. Subsequent peak deconvolution and analysis were performed using the Casa-XPS software.

2.5. Thick film preparation

The thick films were prepared via the screen-printing technique, using the pure and heterostructured samples as-synthesized. First, each sample was mixed with appropriate proportions of α-terpineol and ethyl

Table 1
Sample descriptions and corresponding abbreviations.

Sample	Abbreviation
ZnO rods	ZnO-R
ZnO plates	ZnO-P
NiO nanoplates	NiO
ZnO rods with 20 wt% NiO	ZnO-R-20Ni
ZnO rods with 40 wt% NiO	ZnO-R-40Ni
ZnO plates with 20 wt% NiO	ZnO-P-20Ni
ZnO plates with 40 wt% NiO	ZnO-P-40Ni

cellulose to produce the pastes used for printing, which were then homogenized under an ultrasonic bath for 2 h at room temperature. Alumina substrates (with gold electrodes on the top and platinum heaters on the bottom) were used for deposition, which was performed in an Aurel Automation C920 instrument over an area of 1.3 × 1.7 mm. The deposited films were then heat-treated at 200°C for 2 h and 500°C for 1 h. The heating rate was 1 °C/min. Finally, the deposited films were mounted on TO39 supports and connected to the measurement system within the gas-sensing test chamber. For simplicity, abbreviations were assigned for each sample based on its characteristics, as described in Table 1.

2.6. Gas sensing characterization

The sensors were electrically characterized in a hermetically closed chamber under a total flow of 500 sccm. Synthetic air (80% N_2 and 20% O_2) was used as the carrier gas. The gases used to test the sensing properties were carbon monoxide (CO, 515 ppm), carbon dioxide (CO_2, 9037 ppm), hydrogen (H_2, 4952 ppm), ethanol (C_2H_5OH, 50.4 ppm), benzene (C_6H_6, 10.2 ppm), acetone (C_3H_6O, 99.7 ppm), and ethylene (C_2H_4, 1010 ppm), all diluted in synthetic air and from certified cylinders with a N5.0 ° of purity (Sapio). These gases were chosen to study the selectivity of materials to different chemical classes. The total flux inside the chamber was controlled by mass flow controllers (MFC), which were also used to dilute the target gas in the carrier gas in appropriate proportions to achieve the desired gas concentrations. Humid air was generated by flushing synthetic air through a bubbler containing deionized water to test the influence of humidity on the measurements. The gas chamber was kept within a thermostatic chamber set to 20.5°C. The temperature and humidity inside the chamber were monitored using a LM35 temperature sensor and a Honeywell HIH-4000 humidity sensor, respectively. Circuit voltages, temperature, and humidity were measured with a 10-channel programmable Keithley K2000 multimeter. Dedicated Thurlby Thandar TTi power supplies provided current to heat the sensors' meander heaters based on the Joule effect.

The gas-sensing response (S) was calculated based on the sensor's conductance in air (G_{air}) and in the presence of the target gas (G_{gas}) using the following definitions:

$$S = \frac{(G_{gas} - G_{air})}{G_{air}} \quad (1)$$

$$S = \frac{(G_{air} - G_{gas})}{G_{gas}} \quad (2)$$

Eqs. (1) and (2) were used to calculate the responses for the n-type (ZnO-based) and p-type (NiO) sensors, respectively. Dynamic response plots of CO as a function of temperature were generated to determine the optimal operating temperature. To this end, conductance measurements were conducted over a wide temperature range (approximately 50–500°C) by increasing the sample temperature in ~3–5°C.min^{-1} steps during a progressive voltage increase. The process was completely automated. Two measurements were performed following this procedure: one in synthetic air and another one in a mixture of the target gas (CO (50 ppm), C_2H_5OH (1 ppm), and different humidity levels) with synthetic air. Subsequently, their responses were calculated from their conductance by applying Eqs. 1 and 2, yielding a continuous response as a function of temperature. Finally, their optimal operating temperature was determined as the temperature at which the response was the highest. To complement the dynamic response data, conventional isothermal measurements were conducted from 200 to 450°C, in 25°C increments. In these tests, the sensors were first stabilized at the targeted temperature in synthetic air. Afterward, 50 ppm of CO was fluxed into the chamber, and the sensor responses were calculated using Eqs. 1 and 2. This process was also used to evaluate sensor performance (responses and selectivity) at the determined optimal operating temperatures for CO and ethanol.

The gas-sensing performance was evaluated by exposing the samples to a variety of gases, including CO, CO_2, H_2, C_2H_5OH, C_3H_6O, C_6H_6, and C_2H_4. Herein, we focused on the detection of CO and C_2H_5OH due to their importance in air quality assessment, leak detection, and breath analysis. To assess the sensor's selectivity, we tested its response against common interfering gases. Specifically, for CO detection, we investigated CO_2 and H_2 as potential interferents, as they are frequently present alongside CO in industrial emissions and closed environments. For ethanol detection, we examined C_3H_6O, C_6H_6, C_2H_4, and CO since they can interfere with breath analysis and environmental monitoring. The concentration used complied with their Threshold Limit Values (TLV), equipment limitation, and sensing behavior. Cross-sensitivity against humidity was also evaluated.

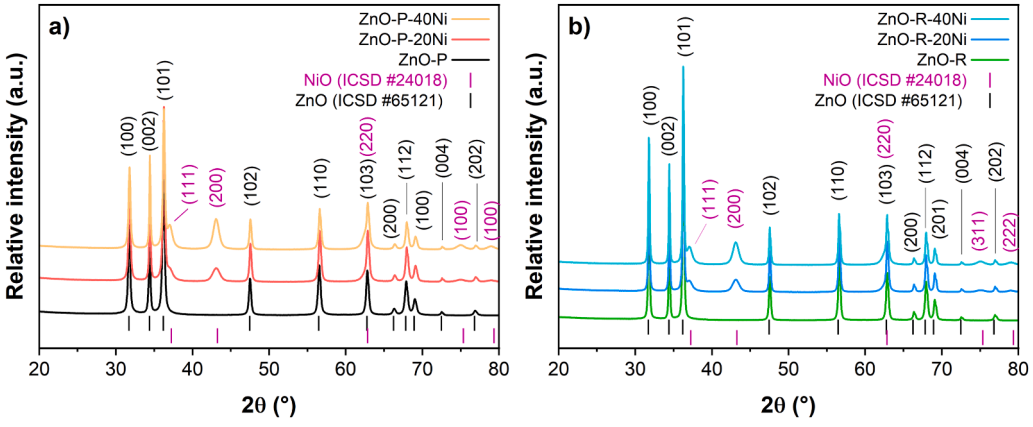

Fig. 1. X-ray diffractometry of the pure ZnO and their respective ZnO/NiO heterostructures for a) plate and b) rod morphologies.

Table 2
Structural parameters obtained for the pure ZnO, NiO, and ZnO/NiO heterostructures via Rietveld refinement analysis.

Sample	Crystallite size (nm)		Cell parameter (Å)		Phase (%)	
	ZnO	NiO	ZnO	NiO	ZnO	NiO
ZnO-P	41.0 (7)	-	a = 3.2535(1) c = 5.2104(1)	-	100	-
ZnO-P-20Ni	53(1)	6.4(1)	a = 3.2510(1) c = 5.2070(1)	4.1991(2)	75.7	24.3
ZnO-P-40Ni	52(1)	8.1(1)	a = 3.2509(1) c = 5.2067(1)	4.1999(1)	58.2	41.8
ZnO-R	189(5)	-	a = 3.2511(1) c = 5.2089(1)	-	100	-
ZnO-R-20Ni	197(4)	7.8(1)	a = 3.2507(1) c = 5.2074(1)	4.1962(1)	75.2	24.8
ZnO-R-40Ni	218(7)	8.7(1)	a = 3.2507(1) c = 5.2073(1)	4.1971(1)	62.1	37.9
NiO	-	7.43 (6)	-	4.18139 (8)	-	100

3. Results

3.1. X-ray diffractometry (XRD)

The XRD patterns of the pure and heterostructured samples are shown in Fig. 1. The reflections were indexed to the wurtzite phase of ZnO (ICSD #65121, shown in brown) [26] and the fluorite-type cubic phase of NiO (ICSD #24018, shown in purple) [27]. Reflections associated with impurity phases were not observed for any sample. It is worth noticing that ZnO-P and ZnO-R display a textured pattern regarding reflections (100) and (002) (Figure S1), which correspond to the planes $(10\bar{1}0)$ and (0001) in the hexagonal setting, respectively [28]. Sample texturing in XRD can be affected by factors related to the analysis procedure and intrinsic properties of the materials, such as sample handling and preparation, preferential orientation, and morphology. In our case, the different intensities of reflections (100) and (002) for ZnO-P and ZnO-R can be assigned to their different morphologies. The natural alignment of plates and rods causes a preferential orientation that induces a higher peak intensity for planes (100) for rod morphologies and (002) for the plates. This trend was also observed in other works discussing ZnO morphologies, where a disproportionate exposure of facets was reported [29–32]. For instance, the XRD pattern of vertically aligned ZnO nanorods synthesized over ZnO-seeded silica substrates showed a predominant (002) reflection [33]. In contrast, when the nanorods lacked a fixed orientation, (100) seemed to be more intense than (002) [32] since the lateral plane of the rods dominated the reflections in the XRD pattern.

For the ZnO/NiO heterostructures, three characteristics are noteworthy: i) the preferential orientation observed for ZnO-P and ZnO-R was preserved for all samples, ii) both wurtzite and fluorite-type phases of ZnO and NiO, respectively, could be detected, and iii) the intensity of the reflections indexed to the NiO phase increased with the increase in the NiO wt%. Indeed, the calculated percentages of the NiO phase for each heterostructure obtained via Rietveld refinement (Figures S2 and S3) were 24.3%, 41.8%, 24.8%, and 37.8% for the ZnO-P-20Ni, ZnO-P-40Ni, ZnO-R-20Ni, and ZnO-R-40Ni heterostructures, respectively. The refinement data in Table 2 also illustrate the crystallite sizes and unit-cell parameters for each phase. The crystallite size of ZnO-P is smaller than that of ZnO-R, which is consistent with their FE-SEM analysis discussed later in Section 3.2. In addition, the crystallite sizes increased for both ZnO-P and ZnO-R in the heterostructures, probably induced by the heat treatment used to synthesize them. No significant changes were observed regarding the lattice parameters for the ZnO phase in the heterostructures. Moreover, the lattice parameter of the NiO nanostructures synthesized on top of the ZnO morphologies increased compared to the pure NiO sample. This effect is probably associated with the lattice mismatch between the base ZnO morphology and NiO, which induces a larger lattice parameter for the NiO phase. The XRD pattern and Rietveld refinement for the pure NiO samples are shown in Figure S4.

3.2. Field-emission scanning electron microscopy (FE-SEM)

The FE-SEM images in Fig. 2 illustrate the morphological characteristics of the pure ZnO and the ZnO/NiO heterostructures. By adjusting the Zn^{2+}:OH^{-} molar ratio, two distinct morphologies were obtained for pure ZnO: plates at a ratio of 1:5 (Fig. 2a) and rods at a ratio of 1:10 (Fig. 2d). The ZnO-P plates featured an average top area of 0.03 μm^2 (IQR of 0.012–0.073 μm^2) and a nanometric thickness of about 26 ± 6 nm (Figure S5). The top area distribution of the plates showed a

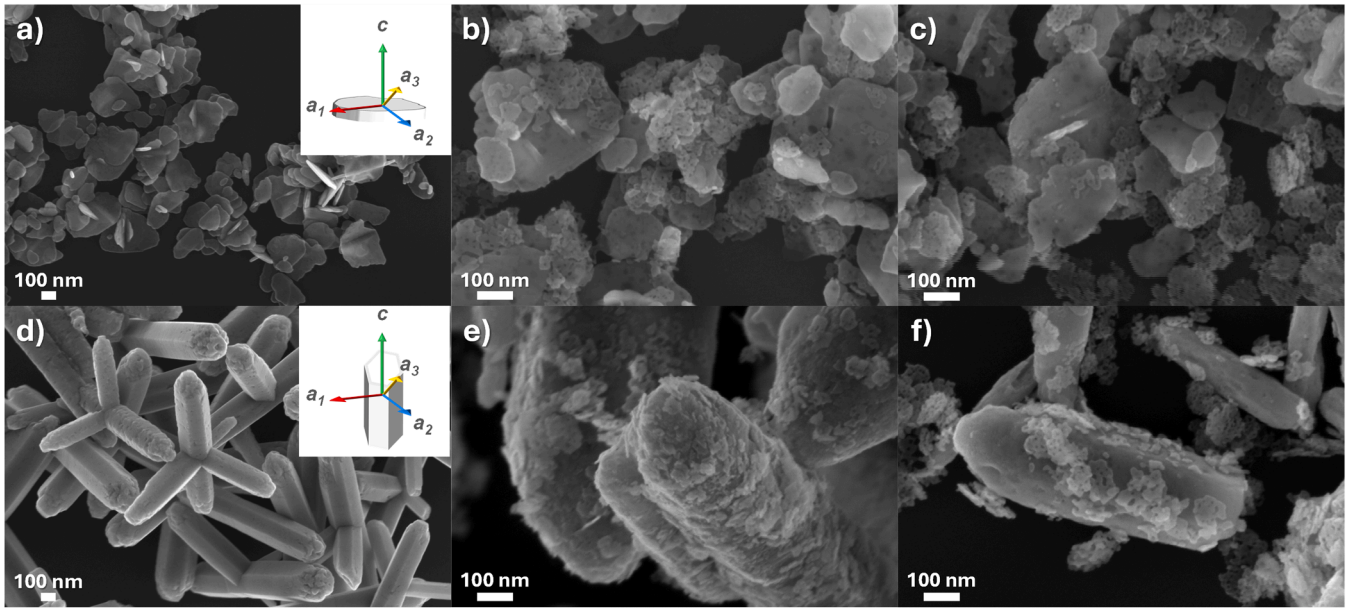

Fig. 2. Field-emission scanning electron microscopy (FE-SEM) of pure ZnO morphologies and their respective ZnO/NiO heterostructures: a) ZnO-P, b) ZnO-P-20Ni, c) ZnO-P-40 Ni, d) ZnO-R, e) ZnO-R-20Ni, and f) ZnO-R-40Ni.

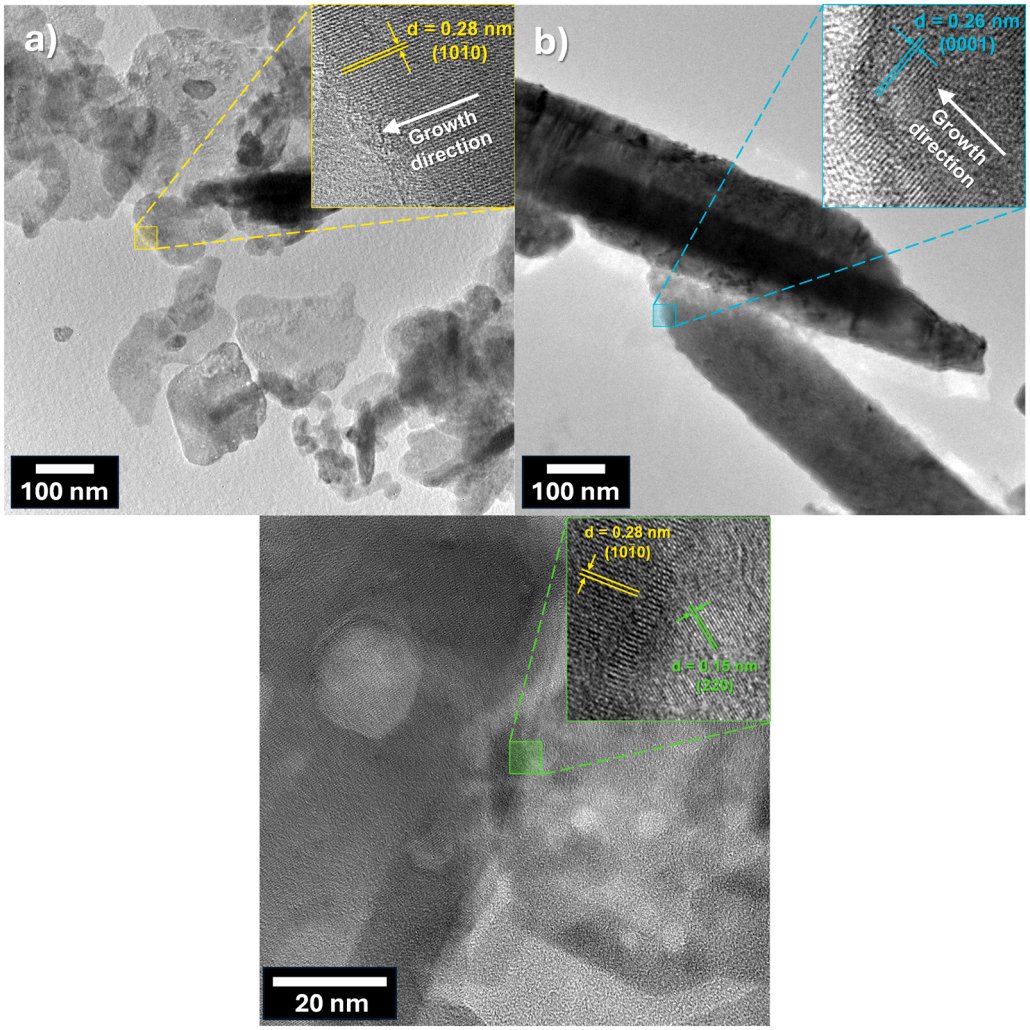

Fig. 3. Transmission electron microscopy (TEM) images of the a) ZnO plates (ZnO-P), b) rods (ZnO-R), and c) ZnO-P-20Ni samples. The insets show the HRTEM images indicating the growth direction and interplanar d-spacing.

positive skewness with a long tail, indicating that although most of their sizes are around the mode, a considerable number have dimensions that exceed it. Such heterogeneity in plate sizes was not observed for thickness, which followed a normal distribution. ZnO-R rods displayed a submicron hexagonal cross-section of 0.30 ± 0.05 μm and a length of 1.6 ± 0.3 μm.

A detailed analysis of nucleation and growth kinetics is essential to understand the ZnO crystal growth processes under different Zn^{2+}:OH^- molar ratios. The growth units consist of zinc hydroxide species, which serve as fundamental intermediates in the wet chemical synthesis of ZnO and are ultimately converted into ZnO crystals. The possible zinc hydroxide species can be described as $[Zn(OH)_n]^{(2-n)}$ (n = 1, 2, 3, 4), forming upon the addition of OH^- to a solution containing dissolved Zn^{2+} cations:

$$Zn^{2+} + n(OH^-) \rightarrow [Zn(OH)_n]^{(2-n)} \quad (3)$$

The stability of these species depends on several factors, such as the concentration of the Zn^{2+}/OH^- species, temperature, pH, etc [34]. Prior research indicates that increasing the solution pH progressively shifts the predominant zinc hydroxide species from $Zn(OH)^+$ to $[Zn(OH)_4]^{2-}$ [35–37]. In the synthesis of ZnO-P, the addition of OH^- (1:5 molar ratio) to the Zn^{2+} solution yielded a cloudy white mixture, probably due to the precipitation of $Zn(OH)_2$ (Eq. 4). On the other hand, adding NaOH at a 1:10 molar ratio (for ZnO-R) resulted in a clear solution, which later also turned white upon homogenization. This reaction can be associated with the transformation of $Zn(OH)_2$ into $[Zn(OH)_4]^{2-}$ (Eq. 5), which is transparent in aqueous solutions. Consequently, the higher initial Zn^{2+} concentration in the ZnO-P synthesis probably displaced the equilibrium, favoring the formation of more $Zn(OH)_2$ precipitates. During synthesis, the zinc hydroxide species undergoes dehydration, forming ZnO crystals according to Eqs. 6 and 7.

$$Zn^{2+} + 2(OH^-) \rightarrow Zn(OH)_2 \quad (4)$$

$$Zn(OH)_2 + 2(OH^-) \rightarrow [Zn(OH)_4]^{2-} \quad (5)$$

$$Zn(OH)_2 \rightarrow ZnO + H_2O \quad (6)$$

$$[Zn(OH)_4]^{2-} \rightarrow ZnO + H_2O + 2OH^- \quad (7)$$

Thus, we propose that the ZnO crystallization can be divided into three mechanisms. In the first, $[OH^-]$ is low, and the more reactive {0001} surfaces of ZnO will be preferentially consumed during the synthesis to minimize surface energy [38]. This process promotes crystal growth along the [0001] direction (c-axis) and forms rod-like morphologies, as commonly reported in the literature for synthesis performed under mildly basic pH values [32,39–41]. In the second, high $[OH^-]$ can induce the adsorption of OH^- on {0001} polar surfaces, stabilizing them by lowering their energy and thus suppressing growth in the [0001] direction [38]. Consequently, crystallization is favored in $< 10\bar{1}0 >$ directions (a_1, a_2, and a_3, perpendicular to the c-axis) [39],

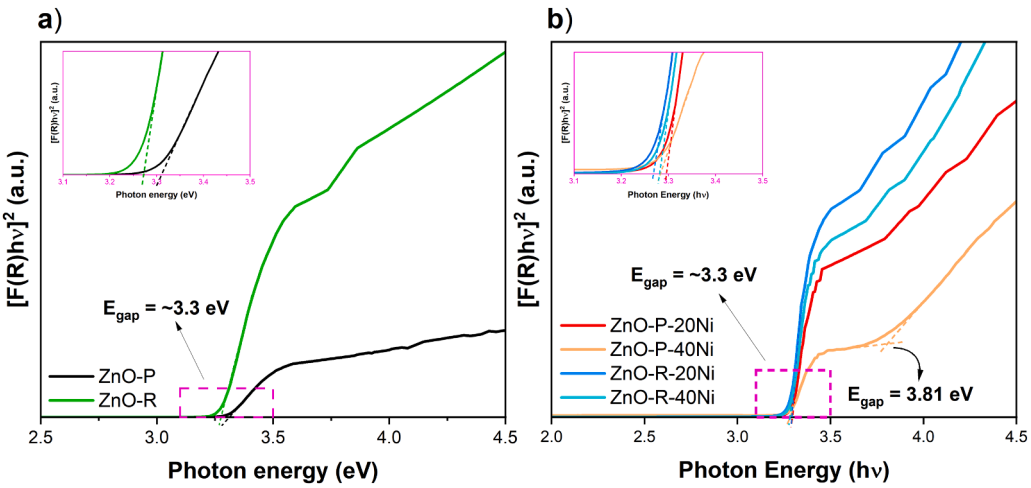

Fig. 4. Bandgap energy (E_{gap}) estimation for the a) pure ZnO morphologies and b) ZnO/NiO heterostructures. The insets show an amplified view of the band edge absorption.

leading to the nanoplates shown in Fig. 2a. In the third, further increasing [OH^-] induces the formation of $[Zn(OH)_4]^{2-}$ species, which likely act as a new growth unit, preferentially resulting in the formation of ZnO rods, as shown in Fig. 2d. One possibility is that the negatively charged $[Zn(OH)_4]^{2-}$ species react with the polar planes of ZnO rather than with non-polar {10$\bar{1}$0} surfaces, resulting in the crystal growth along the [0001] direction [42]. Thus, the ZnO plates consist of reactive polar {0001} surfaces on the top and bottom, with less reactive non-polar {10$\bar{1}$0} surfaces on the sides. On the other hand, the rods display the {10$\bar{1}$0} surfaces along their longitudinal direction, with the {0001} surfaces on their tips [28].

The FE-SEM images of the heterostructures are shown in Figs. 2b-c and 2e-f. No significant differences were noted for the base ZnO plates and rods after the synthesis of the heterostructures. For ZnO-P-20Ni (Fig. 2b) and ZnO-P-40Ni (Fig. 2c), the base ZnO plates are distinguished by their larger size compared with the NiO structures, which are the smaller, porous disks localized on top of the ZnO plates (the pure NiO nanostructures are shown in Figure S6). For the ZnO-R-20Ni (Fig. 2e) and ZnO-R-40Ni (Fig. 2f), the NiO porous plates were distributed over the surface of the rods. These images show that the NiO structures were effectively synthesized over the base ZnO structures without inducing morphological changes. The elemental mapping shown in Figure S7 indicates that the NiO structures were mostly homogenously distributed, with minor agglomeration in some sample regions.

3.3. High-resolution transmission electron microscopy (HRTEM)

HRTEM was performed to investigate the morphologies' surfaces and confirm their growth direction. The interplanar spacing (d) of 0.28 nm for the plate morphology (Fig. 3a) corresponds to the {10$\bar{1}$0} plane family. As explained previously, these planes are parallel to the [0001] direction. Therefore, observing these fringes in Fig. 3a indicates that the growth direction is indeed in the $< 10\bar{1}0 >$ direction, and that the top and bottom facets exhibited by the plates are composed of the {0001} planes (perpendicular to [0001]). The opposite was observed for the rod morphology (Fig. 3b): the fringes identified in the HRTEM inset correspond to {0001} planes (d spacing of 0.26 nm), indicating that the growth direction is [0001] and that the rods exhibit {10$\bar{1}$0} planes on their longitudinal facets. These observations corroborate the results of the XRD and SEM analysis and are consistent with theoretical and experimental studies [43,44]. To investigate the interface between the ZnO and NiO phases, HRTEM analysis was performed on the ZnO-P-20Ni sample, as shown in Fig. 3c. The ZnO plates are on the left, while the NiO appears as a hexagonal plate on the right. Due to the 2D nature of both morphologies, they tend to align horizontally on the grid, making it difficult to isolate the cross-section of the ZnO/NiO interface. However, lattice fringes corresponding to both ZnO (d = 0.28 nm, {10$\bar{1}$0}) and NiO (d = 0.15 nm, {220}) planes were identified within the same region. The preservation of both d-spacings at the contact area, without lattice distortion or intermediate layers, suggests that no significant diffusion or secondary phase formation occurred at the interface, confirming the structural integrity of the heterojunction.

3.4. Diffuse reflectance Ultraviolet-visible spectroscopy (UV-Vis DRS)

Fig. 4 shows the estimated band gap energies of the pure and heterostructured samples. All ZnO-based samples, including the heterostructures, presented a band gap of about 3.3 eV, with no significant variation regardless of morphology, heterostructure, and NiO wt% content. These values are consistent with the band gap energy of ZnO usually found in the literature [45–47]. These results indicate that no significant modification occurred in the base ZnO band structure upon the heterostructure formation. Apart from the band edge absorption for the ZnO phase, a second absorption edge was found for the ZnO-P-40Ni sample, which was attributed to the NiO phase. Indeed, the band gap of ~3.8 eV is within the range commonly found for NiO samples [48–50]. The pure NiO sample presented a band gap energy of ~3.55 eV (Figure S9), which is slightly smaller than the NiO phase in the heterostructure. This difference can be attributed to the effect of the base ZnO structure, which can induce lattice strain in the NiO phase due to the lattice mismatch between the ZnO and NiO, possibly modifying its band structure and, consequently, the band gap [51–54]. Indeed, as discussed in the XRD analysis, the lattice parameter of NiO in the heterostructure increased compared to the pure sample. This absorption region was not clearly defined for the other heterostructures, especially the ones based on ZnO-R, and thus could not be determined.

3.5. Gas sensing characterization

3.5.1. Operating temperature determination

The sensor's optimal operating temperatures (T_{op}) for CO and ethanol were determined from dynamic response curves measured as a function of temperature, as depicted in Fig. 5. This approach allows the determination of the optimal T_{op} with greater resolution, as it measures the response under continuous, automated temperature variation rather than at fixed, predetermined isothermal temperatures, which is time-consuming. The reliability of this method was further validated by comparing the obtained T_{op} values with those from the isothermal

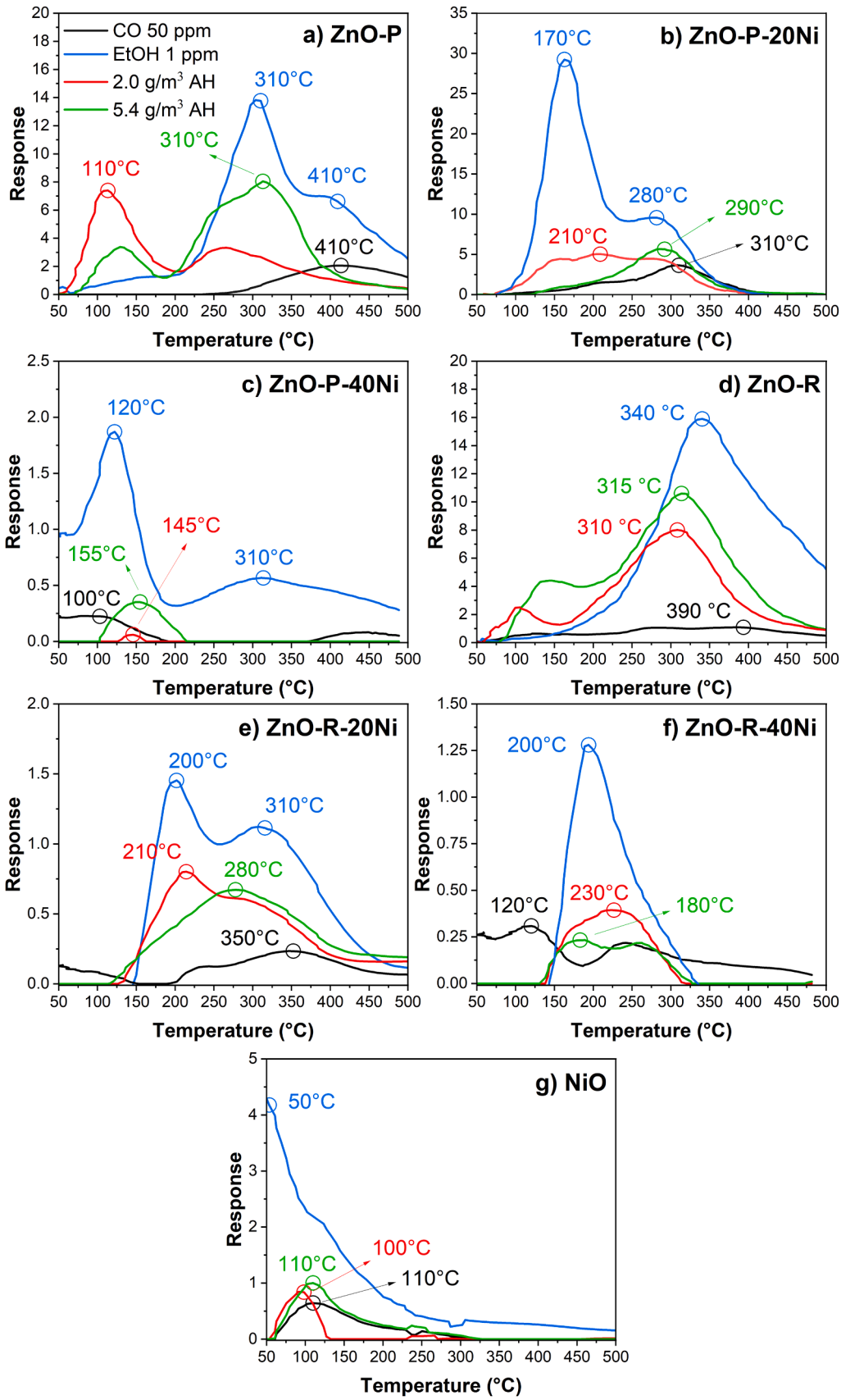

Fig. 5. Response in function of temperature plots for each sensor toward carbon monoxide (50 ppm), ethanol (1 ppm), and two absolute humidity levels (2.0 and 5.4 g/m^3, set at ~22°C inside the chamber).

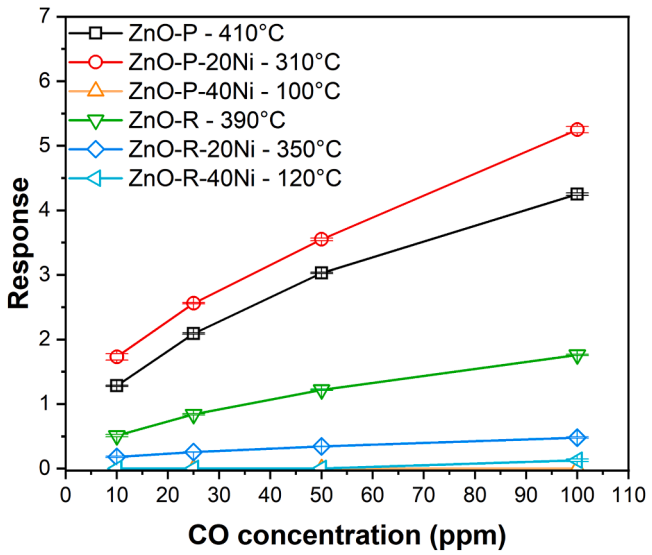

Fig. 6. Sensor's response at their optimal operating temperature to CO as a function of the CO concentration. The connecting lines are provided as a visual guide for the data points.

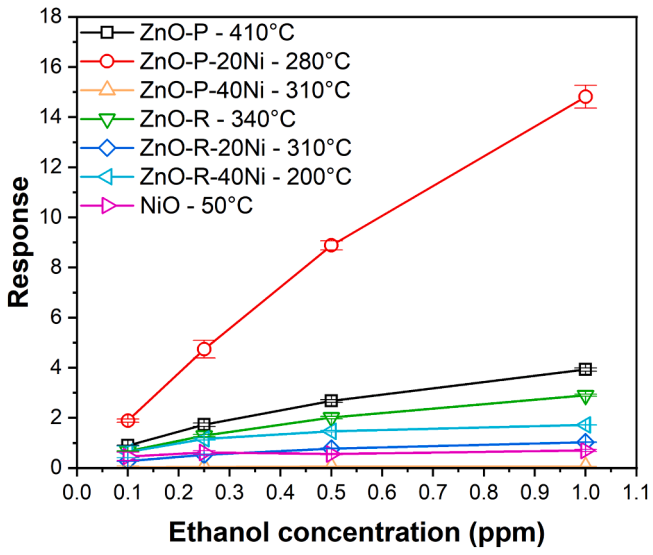

Fig. 7. Sensor's response at their optimal operating temperature toward ethanol in function of the ethanol concentration. The connecting lines are provided as a visual guide for the data points.

Table 3
Sensors' responses to different CO concentrations at their optimal operating temperature for CO. Measurements were performed in triplicate. The sensors with no values presented no measurable response at the specific concentration.

Sample	Response to CO			
	10 ppm	25 ppm	50 ppm	100 ppm
ZnO-P	1.28 ± 0.01	2.09 ± 0.01	3.03 ± 0.01	4.25 ± 0.02
ZnO-P-20Ni	1.73 ± 0.05	2.56 ± 0.01	3.55 ± 0.02	5.25 ± 0.05
ZnO-P-40Ni	-	-	-	-
ZnO-R	0.51 ± 0.02	0.84 ± 0.01	1.22 ± 0.01	1.76 ± 0.01
ZnO-R-20Ni	0.18 ± 0.01	0.254 ± 0.001	0.97 ± 1.08	0.341 ± 0.002
ZnO-R-40Ni	-	-	-	0.13 ± 0.02
NiO	-	-	-	-

procedure for CO, as presented in Figure S10. CO was selected for this validation due to its simple, well-defined reaction kinetics, which enabled a fundamental understanding of the samples' performance under both dynamic and isothermal testing conditions.

For the sensors based on plate morphologies (Fig. 5a-c), the formation of heterostructures with NiO decreased the optimal T_{op} toward CO by 100°C, from 410°C for ZnO-P (Fig. 5a) to 310°C for ZnO-P-20Ni (Fig. 5b). For ZnO-P-40Ni (Fig. 5c), the increased wt% of NiO reduced the T_{op} to 100°C; however, the response was substantially reduced. For the sensors based on rod morphologies (Fig. 5d-e), the formation of heterostructures with NiO was detrimental to the performance of ZnO-R, yielding much lower responses. Nevertheless, as with the heterostructures formed with ZnO plates, increasing the wt% of NiO decreased the optimal T_{op} compared with the pure ZnO-R.

Under ethanol exposure, most sensors exhibited a similar behavior to that observed with CO: the heterostructured samples consistently reduced the optimal operating temperature (T_{op}) compared to their pure counterparts (ZnO-P and ZnO-R). However, this came at the cost of impaired sensitivity for ZnO-P-40Ni (Fig. 5c), ZnO-R-20Ni (Fig. 5e), and ZnO-R-40Ni (Fig. 5f). An exception was the ZnO-P-20Ni sample (Fig. 5b), which demonstrated both increased sensitivity and a simultaneous reduction in its optimal T_{op}. Among all sensors, pure NiO showed the lowest optimal T_{op}, detecting ethanol near room temperature (Fig. 5g). Moreover, most sensors exhibited two temperature points at which sensitivity to ethanol was higher, which might correspond to two different processes (dehydrogenation and dehydration) involved in the sensing mechanisms of ethanol [55]. This will be discussed later in the text. Fig. 5 also shows the sensors' response to two humidity levels (absolute humidity of 2.0 and 5.4 g/m^3). These curves are crucial because they show at which temperature ranges water molecules have a higher interference potential against the other gases. This discussion is presented in Section 3.5.4.

3.5.2. Gas concentration evaluation

Fig. 6 depicts the relationship between CO concentration and sensor response at the determined optimal operating temperatures in Fig. 5, with supporting numerical data in Table 3. The ZnO-P-20Ni heterostructure achieved the highest sensitivity to CO across all tested concentrations, indicating that the ZnO/NiO heterostructure effectively enhanced CO sensitivity by approximately 25% while simultaneously lowering the required operating temperature. However, further increasing the NiO wt% results in a complete degradation of sensing capabilities, as evidenced by the ZnO-P-40Ni sample. Interestingly, a different behavior was observed for the sensors based on rod morphologies, where heterostructure formation reduced CO sensitivity by roughly 70% compared to ZnO-R, with further increases in NiO wt% amplifying this effect. Moreover, the pure NiO sensor exhibited a significant limitation, failing to recover from CO exposure and resulting in cumulative baseline drift proportional to the number of CO injections (Figure S11). This behavior of the NiO sensor is probably associated with the operating temperature, which was not high enough to promote CO desorption. Interestingly, no baseline drift was observed for ZnO-P-40Ni and ZnO-R-40Ni, which also operated at similar temperatures.

For ethanol, as previously discussed in Fig. 5, most sensors indicated

Table 4
Sensors' responses to different ethanol concentrations at their optimal operating temperatures.

Sample	Response to Ethanol			
	0.1 ppm	0.25 ppm	0.5 ppm	1 ppm
ZnO-P	0.89 ± 0.01	1.73 ± 0.07	2.68 ± 0.06	3.93 ± 0.06
ZnO-P-20Ni	1.89 ± 0.07	4.74 ± 0.35	8.88 ± 0.18	14.81 ± 0.45
ZnO-P-40Ni	-	-	-	-
ZnO-R	0.67 ± 0.01	1.29 ± 0.05	2.01 ± 0.05	2.90 ± 0.04
ZnO-R-20Ni	0.28 ± 0.01	0.53 ± 0.02	0.77 ± 0.02	1.02 ± 0.01
ZnO-R-40Ni	0.64 ± 0.23	1.16 ± 0.04	1.46 ± 0.03	1.72 ± 0.01
NiO	0.46 ± 0.17	0.62 ± 0.08	0.55 ± 0.02	0.70 ± 0.04

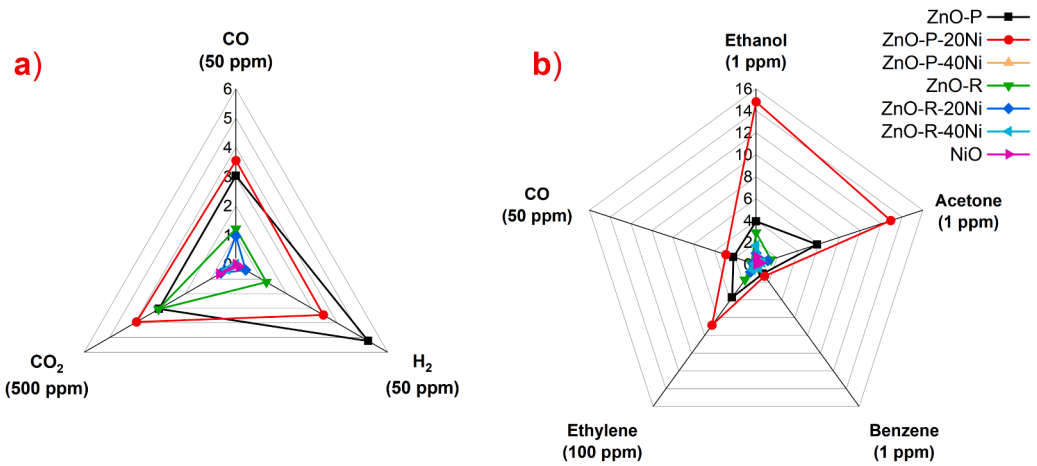

Fig. 8. Selectivity tests performed for (a) CO against 500 ppm of CO_2 and 50 ppm of H_2 and for (b) ethanol against 1 ppm of acetone, 1 ppm of benzene, 100 ppm of ethylene, and 50 ppm of CO. The sensors' operating temperature in (a) and (b) were the same as in Figs. 6 and 7, respectively.

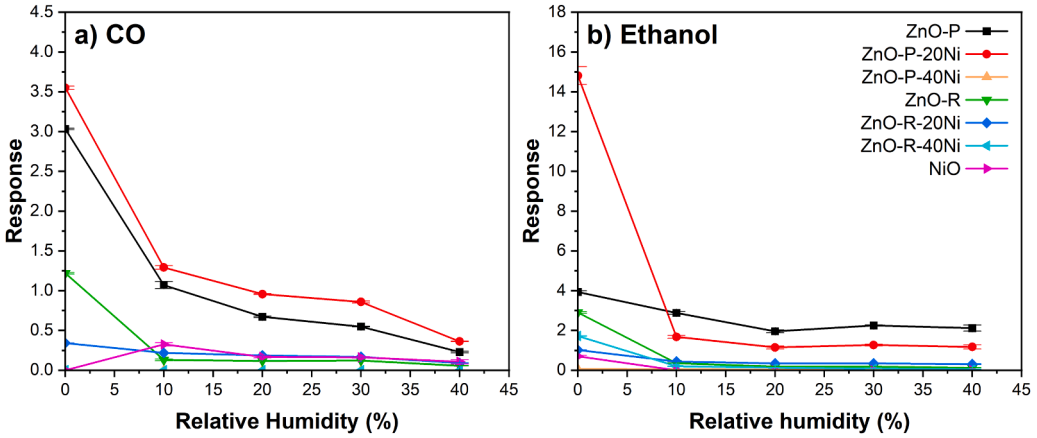

Fig. 9. Effect of relative humidity on sensor response to a) 50 ppm of carbon monoxide (CO) and b) 1 ppm of ethanol (C_2H_5OH). The sensors' operating temperature in (a) and (b) were the same as in Figs. 6 and 7, respectively. Relative humidity setting temperature of ~27°C inside the test chamber.

two temperatures of interest for performing the sensing measurements. The sensors exhibited higher sensitivity at lower operating temperatures, especially the ZnO-P-20Ni sensor, which showed a significantly higher response to 1 ppm of ethanol (Figure S12). However, the sensors were unable to reach saturation and/or return to their initial conditions, likely due to a slow reaction and desorption of the gas molecules, respectively, which is an important limitation for them. Therefore, the next-best operating temperature was selected for the sensing measurements because the sensors at this temperature displayed the characteristic response and recovery behavior (Figure S13). The sensors' performance at varying ethanol concentrations is shown in Fig. 7 and summarized in Table 4. In this case, the sensitivity to ethanol followed a trend similar to that observed under CO exposure: the ZnO-P-20Ni heterostructure showed higher sensitivity than ZnO-P, while ZnO-P-40Ni exhibited negligible responses. For the rod-based sensors, the heterostructure formation negatively impacted the performance of ZnO-R. Notably, the sensitivity of ZnO-P-20Ni to ethanol was substantially higher than that of the pure ZnO-P and ZnO-R sensors; approximately 275% and 410% higher, respectively. It is also worth emphasizing the high sensitivity of the sensors, as the tested concentrations ranged from ppb levels (100 ppb, or 0.1 ppm) to 1 ppm.

3.5.3. *Selectivity tests*

The sensors' selectivity towards CO and ethanol was assessed by testing the interference of CO_2 and H_2 on CO (Fig. 8a), and acetone, benzene, ethylene, and CO on ethanol (Fig. 8b). Among all sensors, the ones that showed the best performance were the pure ZnO-P and ZnO-R and the ZnO-P-20Ni heterostructure. For CO (Fig. 8a), the ZnO-P-20Ni heterostructure presented no selectivity towards any of the gases (maximum response difference of ~10% in respect to CO_2), while the ZnO-P and ZnO-R sensors displayed a higher selectivity for H_2 (~73% higher than CO) and CO_2 (~150% higher than CO), respectively. Conversely, for ethanol (Fig. 8b), the heterostructure showed higher selectivity toward ethanol and acetone, with maximum differences of ~120% and ~90% relative to ethylene, respectively. The ZnO-P sensor displayed lower responses with slight selectivity toward ethanol and acetone. For ZnO-R, the responses indicated higher selectivity for ethanol and ethylene, with the lowest response among the three samples. An interesting feature of these measurements is that ZnO-R, which displays non-polar $(10\bar{1}0)$ surfaces, showed an increased sensitivity towards non-polar molecules, such as carbon dioxide (CO_2) and ethylene (C_2H_4).

3.5.4. *Humidity effect*

Fig. 9 illustrates the influence of humidity on the gas-sensing performance of the sensors for CO and ethanol. In both cases, increasing relative humidity decreased sensitivity; however, the nature and extent of this interference were gas-dependent. For CO (Fig. 9a), the sensors experienced a steep decrease of the response from dry air to 10% RH (about 65% for ZnO-P and ZnO-P-20Ni, and ~90% for ZnO-R), with

further increases in the RH% continuously decreasing the response to CO. Nevertheless, the ZnO-P-20Ni heterostructure performed better than the pure ZnO-P sensor in all RH% tested, and no relevant response was observed for the other sensors.

A different trend was observed for ethanol (Fig. 9b). Under humid conditions, the ZnO-P-20Ni heterostructure exhibited a substantially greater decrease in ethanol response compared to the ZnO-P sensor. At 10% RH, the response of ZnO-P-20Ni decreased by approximately 90% relative to its response in dry air, whereas ZnO-P showed a decrease of only ~25%, indicating that ZnO-P retains better sensitivity under humid conditions. Beyond 10% RH, both sensors showed relatively stable ethanol responses, *i.e.*, RH had only a slight impact on their performance. This stable behavior is a promising result, as it indicates that further variations in relative humidity do not significantly affect sensor performance, a highly desirable characteristic for practical gas-sensing applications in real-world environments.

These results directly correlate with those presented in Fig. 5. For the ZnO-P-20Ni heterostructure, humidity sensitivity was generally lower than that of the ZnO-P sensor across the entire temperature range tested, indicating that heterostructure formation effectively suppressed the overall humidity effect. This analysis is further corroborated by investigating their response to humidity around their maxima (about 300°C, represented by the green and red curves in Fig. 5), as shown in Figure S14. The heterostructure displayed a consistently lower RH response than both ZnO-R and ZnO-P, while ZnO-R was more susceptible to humidity than ZnO-P. However, for the ZnO-P-20Ni heterostructure, the maximum sensitivity to both ethanol and humidity converged within a narrow temperature range, which likely contributed to the pronounced decrease in ethanol sensitivity under humid conditions. In contrast, for the ZnO-P sample, the temperature at which ethanol sensitivity was best coincided with a region where its overall humidity sensitivity was decreasing. This offset may account for the smaller reduction in ethanol sensitivity observed for ZnO-P, as shown in Fig. 8b. On the other hand, the heterostructure showed a higher response than the ZnO-P sample under CO exposure, indicating better performance in both dry and humid conditions, despite the close proximity of their sensitivity maxima for CO and humidity. This analysis suggests that the approach presented in Fig. 5 is a valuable tool for determining optimal operating temperatures that balance sensitivity to the target gas with the influence of humidity and interfering gases. Although this strategy did not achieve the same level of optimization for CO as for ethanol, it still provides a meaningful framework for sensor design and can be extended to a broader range of target gases and experimental conditions.

3.5.5. Sensing mechanisms

Before delving into the specific sensing mechanisms that influence each sensor's performance, it is essential to highlight the size difference between the base ZnO-P and ZnO-R samples. The average size of ZnO-R rods is significantly greater than that of ZnO-P plates, as clearly shown in the FE-SEM images in Fig. 2. This observation was further supported by Rietveld refinement analysis, which confirmed that the crystallite size of the ZnO-R rods (189 nm) is larger than that of the ZnO-P plates (41 nm). It is well established in the literature that particle/crystallite dimensions strongly affect sensing performance, particularly the sensitivity to the target gas [56]; thus, this parameter must be considered. As revealed by the sensing analysis, ZnO-P generally performed better than ZnO-R under most testing conditions, and the smaller particle size probably contributed to this enhanced performance. However, a comparable response was observed for CO_2, and ZnO-R outperformed ZnO-P in humidity sensitivity. Despite the larger ZnO-R crystallite size, their performance in these tests suggests that morphology and surface reaction mechanisms play significant roles.

Morphology-wise, the ZnO-P plates consist of two polar planes terminated with Zn or O atoms, hereby denoted as (0001)-Zn and $(000\bar{1})$-O, respectively, with lateral facets consisting of nonpolar $\{10\bar{1}0\}$ planes. The ZnO-R rods feature longitudinal hexagonal facets that are also composed of the nonpolar $\{10\bar{1}0\}$ planes, while their tips display polar (0001)-Zn and $(000\bar{1})$-O. Nonpolar $(10\bar{1}0)$ has Zn and O atoms alternating in the same plane, leading to a charge-balanced arrangement and a theoretical surface energy of 1.12 J/m^2 [57]. In comparison, the polar surfaces consist of stacked alternating layers of Zn and O along the c-axis, ending with either Zn or O atoms. These terminations result in polar planes with higher surface energies compared to $(10\bar{1}0)$, with 2.25 J/m^2 for (0001)-Zn and 2.04 J/m^2 for $(000\bar{1})$-O [57]. Han *et al.* have shown that the gas sensing activity of the $(000\bar{1})$-O surface is limited due to its intrinsic basic nature, weakening their reaction with oxygen species, which are essential to the sensing mechanisms [44]. On the other hand, the (0001)-Zn surface is the most reactive due to the abundance of acid sites (Zn sites). Therefore, each of these surfaces interacts differently with gaseous molecules.

The interaction between humidity and the different ZnO planes is complex [58]. The work of Morimoto and Nagao [59] identified that the $(10\bar{1}0)$ surface, when fully hydroxylated, develops a highly ordered structure of hydrogen-bonded surface hydroxyl groups that yields a uniform and weakly adsorbing surface, promoting high mobility of physisorbed water molecules. Later, studies from Meyer *et al.* further corroborated this idea [60]. The authors reported that water undergoes spontaneous partial dissociation on $(10\bar{1}0)$ surfaces, forming a highly hydroxylated and hydrogen-bonded surface. This dissociation is facilitated by intermolecular interactions among water molecules and occurs with very low activation energy. In contrast, the (0001) surfaces are suggested to have more isolated hydroxyls and lack the structured arrangement that promotes surface mobility, with water adsorbing mainly in molecular form with weaker, less reactive interactions [59,61]. Such differences in the adsorption behavior between $(10\bar{1}0)$ and (0001) surfaces can explain the higher response to humidity of ZnO-R compared to ZnO-P. These reactions persist up to ~300°C (as shown in Fig. 5), reaching a maximum and further decreasing at higher temperatures. Beyond this maximum, response decreases because the surface adsorption/desorption processes become imbalanced. At higher temperatures, the rate of desorption gas molecules and adsorbed oxygen species increases significantly, resulting in reduced interaction between the gas and the surface and consequently impairing the change in electrical conduction that constitutes the sensing signal [7,62]. This result is promising, as it shows that morphological control can address one of the most problematic issues in gas sensors: the cross-interference with humidity.

The gas-sensing mechanisms of chemoresistive sensors are based on the surface-depletion effect, a well-documented phenomenon in the literature [63–65]. In this mechanism, upon exposure to an oxygen atmosphere, O_2 molecules adsorb on the sensing film surface and trap electrons from the conduction band (CB) via the formation of ionized oxygen species (O_2^-, O^-, or O^{2-}, depending on the temperature), creating an electron-depleted layer at the surface. Under these conditions, the contact points between adjacent particles form potential barriers (double Schottky barrier model [64]) that require electrons to overcome a higher energy threshold for electronic transport, thereby increasing the overall resistance of the sensing film. Then, when exposed to a reducing gas (such as CO or ethanol), its molecules will react with the adsorbed oxygen species, releasing the trapped electrons back to the CB, thereby reducing the potential barrier height and increasing the conductance [66,67]. This conductance modulation, driven by different atmospheres, generates the sensing signal. Therefore, based on these mechanisms, the conductance of the ZnO-P samples is expected to be lower than that of the ZnO-R sensors due to: i) the larger size of the ZnO-R particles, which reduces the number of intergranular barriers electrons must overcome for conduction under the same electrode distances; ii) the less pronounced depletion layer effect in larger particles [68,69]; and iii) the smaller particle size of ZnO-P, which results in a higher surface area and thus more surface sites available for adsorption of oxygen species.

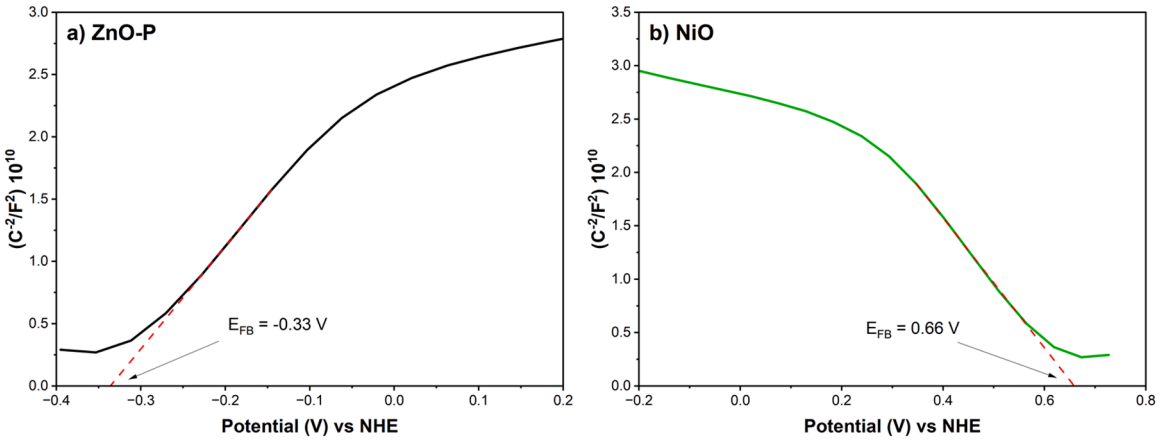

Fig. 10. Mott-Schottky curves of the ZnO-P and NiO samples.

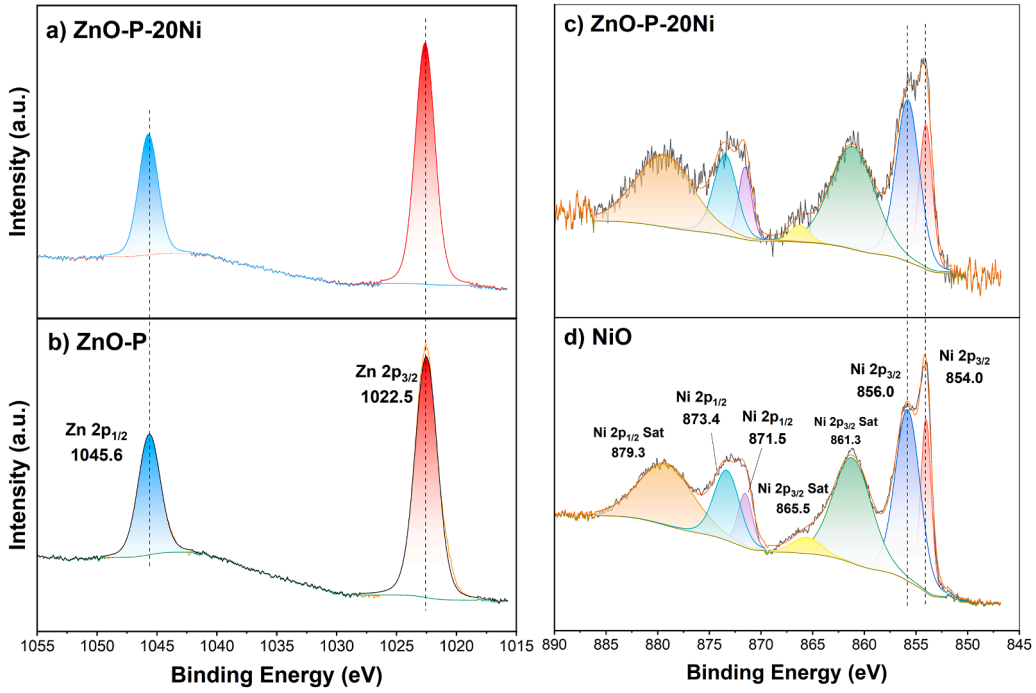

Fig. 11. High-resolution XPS spectra of the Zn 2p state for the a) ZnO-P-20Ni heterostructure and b) ZnO-P, and of the Ni 2p state for the c) ZnO-P-20Ni heterostructure and d) NiO.

Indeed, the ZnO-R sample consistently exhibited a higher baseline conductance in dry air than ZnO-P (6.4×10^{-7} S and 1.7×10^{-7} S, respectively). Consequently, this result indicates a stronger depletion layer effect on the ZnO-P sample. This stronger depletion layer should, in turn, yield a higher response to reducing gases for ZnO-P than for ZnO-R, which was confirmed in the previous analyses.

The band diagram of the ZnO/NiO heterojunction was constructed based on the band gap values calculated in Figure 4 and S9, and on the Mott–Schottky curves shown in Fig. 10. The Mott–Schottky plots show a positive slope for the ZnO-P sample (Fig. 10a) and a negative slope for NiO (Fig. 10b), which confirms their n-type and p-type behavior, respectively. The flat-band potentials (E_{FB}) were determined from the intercepts with the x-axis: being −0.33 V for ZnO-P and 0.66 V for NiO (vs. NHE). For the n-type ZnO-P, the conduction band edge (E_{CB}) is estimated to be approximately 0.1 eV more negative than E_{FB}, resulting in E_{CB} = -0.43 eV. Based on the band gap energy (E_g) of ZnO-P (3.3 eV) and from the relation $E_{VB} = E_{CB} + E_g$ [17,70], the valence band edge (E_{VB}) was calculated to be 2.87 eV. In contrast, for the p-type NiO, E_{VB} is considered as approximately 0.1 eV more positive than E_{FB}, resulting in $E_{VB} = 0.76$ eV. Therefore, based on the NiO band gap (3.55 eV) and the band-edge relationship, the calculated E_{CB} was −2.79 eV. The band-edge energies were then used to construct the band diagram shown in Fig. 11.

High-resolution XPS (Fig. 11) was performed to investigate the electronic environment of the Zn 2p and Ni 2p states in the pure samples and ZnO/NiO heterostructure. The Zn 2p spectrum for pure ZnO-P (Fig. 11b) displayed peaks at 1022.5 eV (Zn $2p_{3/2}$) and 1045.6 eV (Zn $2p_{1/2}$), characteristic of Zn^{2+} [71], which were similar for ZnO-P-20Ni sample (Fig. 11a). In the Ni 2p region, pure NiO (Fig. 11d) exhibited main Ni $2p_{3/2}$ peaks at 854.0 eV and 856.0 eV [72,73], which were also observed for the heterostructure. No significant dislocation of the binding energies was observed after the heterostructure formation at room temperature, indicating that the Zn 2p and Ni 2p states remained similar to their pure counterparts. A shift in the binding energy can indicate the direction of electron migration at the heterojunction [17]. The absence of such a shift in the ZnO-P-20Ni sample might be explained

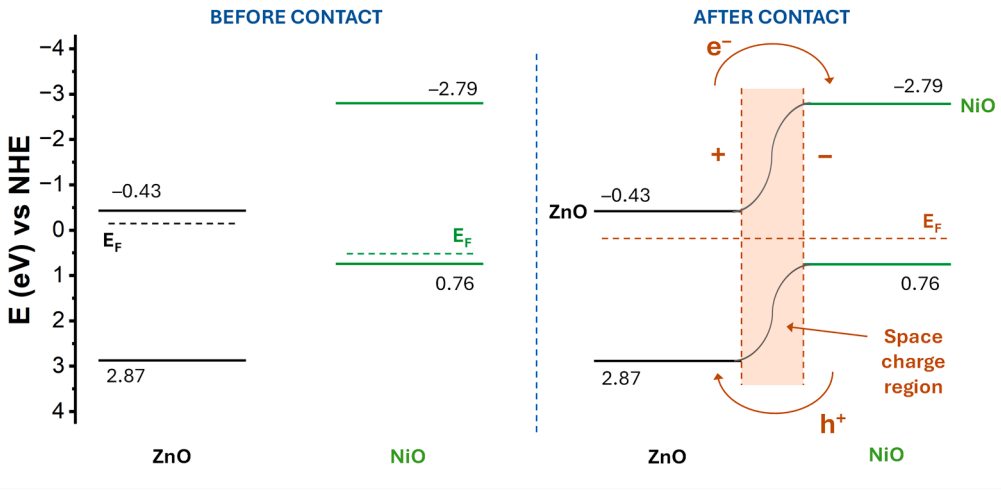

Fig. 12. Band diagram of the NiO and ZnO samples before (a) and after (b) the heterojunction formation.

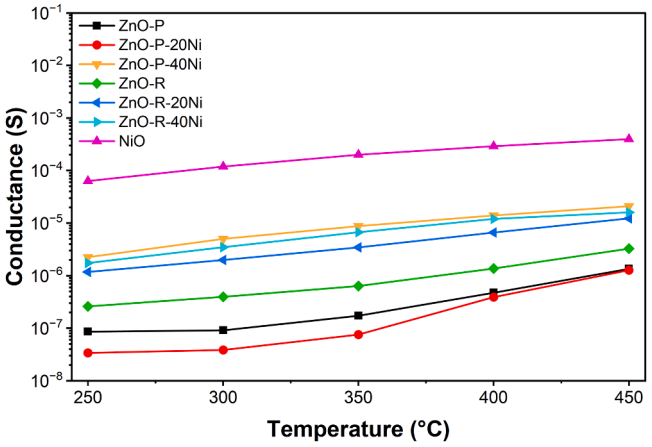

Fig. 13. Conductance in dry air at varying sensors' operating temperatures for the pure ZnO morphologies and their respective ZnO/NiO heterostructures.

by the formation of depleted regions at the p-n interface, which impair electronic migration by creating potential barriers, as observed, which reduced the conductance of the heterostructure (discussed in Fig. 13).

Fig. 12 illustrates the band diagram at the heterojunction between the ZnO-P and NiO samples. Upon formation of a heterojunction, electrons migrate from the semiconductor with the higher Fermi level to the one with the lower Fermi level [74,75]. As an n-type semiconductor, the Fermi level of ZnO is near E_{CB}, whereas for p-type NiO, the Fermi level is closer to the E_{VB}. Consequently, electrons will flow from ZnO to NiO, while holes will follow the opposite path. This migration of charge carriers creates a space charge region (or depletion region) at their interface. Then, the effective formation of the heterojunction should lead to a decrease in the conductance of the heterostructured sample. Indeed, this effect was observed for the ZnO-P-20Ni sample but not for the other heterostructures. This observation suggests that heterojunction formation was either stronger in plate-morphology samples or absent in rod-based samples. Moreover, the large difference in the conduction band edges of the ZnO and NiO samples can explain why electronic migration via XPS was not observable.

As a result, the p-n heterojunction creates a space-charge region at the interface, affecting the conduction pathway in ZnO by increasing the depletion layer, thereby decreasing the conductance. Indeed, the ZnO-P-20Ni heterostructure showed lower conductance compared to its ZnO-P

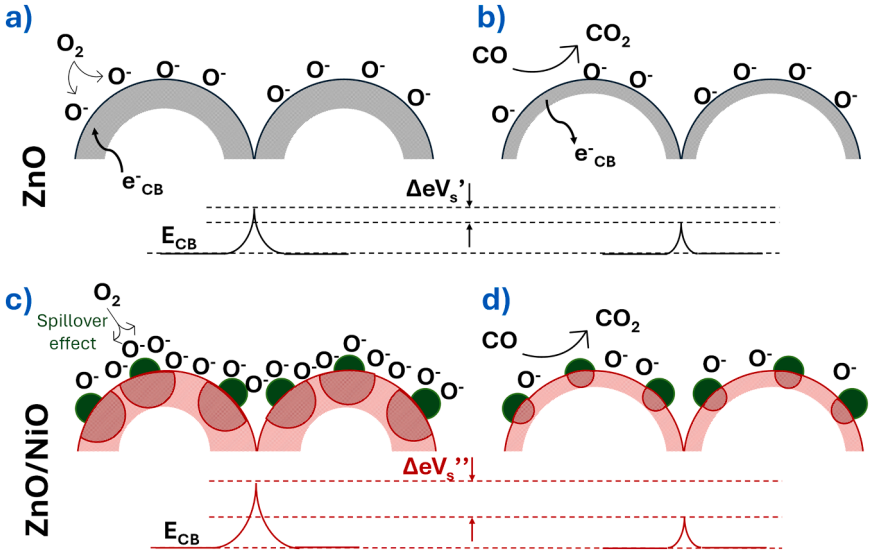

Fig. 14. Schematic illustration of the depletion layer effects on the ZnO-P sensor (in dry air (a) and CO (b)) and on the ZnO-P-20Ni heterostructure (in dry air (c) and CO (d)).

counterpart (7.6×10^{-8} and 1.7×10^{-7} S at 350°C, respectively; Fig. 13), in agreement with the literature [75,76]. However, for all other heterostructures, the conductance increased significantly compared to ZnO-P and ZnO-R. A possible explanation to this behavior is that increasing the NiO concentration also increases the contact between NiO particles, possibly creating an alternative conduction pathway that dominates the signal since the pure NiO sample displayed a conductance three orders of magnitude higher than that of both ZnO-P and ZnO-R (2.0×10^{-4}, 1.7×10^{-7}, and 6.4×10^{-7} S, respectively). A similar behavior was reported by Liu *et al.* [74]. Furthermore, only the ZnO-P-20Ni, not the ZnO-R-20Ni, sample decreased the conductance of its pure counterpart, indicating that morphology played an important role in heterojunction formation. It could be that the ZnO/NiO heterostructure formation on the nonpolar $\{10\bar{1}0\}$ surfaces of ZnO-R was not optimal, whereas it occurred more effectively on the polar (0001)-Zn or $(000\bar{1})$-O surfaces of ZnO-P, as evidenced by the observed decrease in conductance. Therefore, the higher reactivity and electronic density of polar surfaces appear to play a crucial role in facilitating heterojunction formation, indicating that morphology is a key factor in the design of heterostructures [77,78].

Fig. 14 illustrates the possible mechanisms involved in the sensing behavior of the pure ZnO-P and ZnO-P-20Ni heterostructure. As explained previously, for the pure ZnO-P plates, the sensing mechanism relies on modulation of the Schottky barrier height, which controls the sensing signal. Thus, in Fig. 14a, upon exposure to dry air, the formation of oxygen species increases the depletion layer and barrier height, decreasing the conductance. Upon exposure to a reducing gas, such as CO, the reaction with adsorbed oxygen species results in the release of electrons back into the conduction band. This process lowers the barrier height, thereby increasing the material's conductance (Fig. 14b). For the heterostructure, the formation of ZnO/NiO heterojunctions at the surface has an amplifying effect on the depletion layer [79] (Fig. 14c), decreasing the conductance compared to the pure ZnO-P. The mechanisms behind this effect can be attributed to: i) the formation of the heterojunction itself, which increases the depletion layer/barrier height at the ZnO/NiO interface; ii) the adsorption of oxygen species on the NiO surface, which strengthens its p-type characteristics, resulting in an amplification of the depletion layer; and iii) a catalytic effect (spillover effect) of NiO, which increases the rate of reactions at the surface (for both oxygen species and the target gas), thereby increasing the response (as shown in Figs. 6 and 7 for CO and ethanol, respectively). The reduced operating temperature of the heterostructures can also be attributed to the spillover effect (Fig. 5) [75,80,81]. When a reducing gas reacts with the material, the effects described in items (ii) and (iii) are reversed. In the case of an oxidizing gas in (iii), the effects are amplified. This leads to a greater difference in the barrier height within the heterostructure compared to the pure ZnO sample (eVs'' > eVs', Fig. 14d), which ultimately results in the improved response of the ZnO-P-20Ni heterostructure.

4. Conclusions

Zinc oxide samples with plate and rod morphologies were successfully synthesized via the microwave-assisted hydrothermal (MAH) method and subsequently decorated with NiO nanodisks, forming ZnO/NiO heterostructures. $Zn(OH)_2$ was formed at lower OH^- concentrations, favoring plate formation due to suppression of the crystal growth along the [0001] direction by OH^- adsorption, while $[Zn(OH)_2]^{4-}$ species at higher OH^- levels promoted rod formation. NiO was synthesized on ZnO via MAH followed by heat treatment. X-ray diffraction revealed no impurity phases in either pure ZnO or ZnO/NiO samples. Rietveld refinement indicated ~25 wt% and ~40 wt% NiO for each ZnO morphology. FE-SEM confirmed the homogeneous NiO nanodisks distribution on the surface of the base ZnO. ZnO plates exhibited superior responses compared to rods, attributed to their more reactive (0001) surface and stronger depletion layer. However, ZnO rods showed higher humidity sensitivity, likely due to their co-planar Zn–O surface configuration on $(10\bar{1}0)$ planes. The ZnO-P-20Ni heterostructure showed the best overall performance in dry air, with responses up to 275% and 410% higher than pure ZnO plates and rods for 1 ppm of ethanol, respectively. ZnO plates showed the lowest humidity interference (~25% reduction at 40% RH for ethanol). Both ZnO-P-20Ni and pure ZnO plates exhibited slight selectivity toward ethanol and acetone. For ZnO rods, NiO incorporation was detrimental, reducing sensitivity in all cases. This behavior was attributed to a stronger effect of (0001) reactive facets in the ZnO plates, which likely enabled an effective heterojunction formation at the ZnO/NiO interface. In contrast, samples with 40 wt% NiO and both rod-based heterostructures likely formed alternative conduction pathways via NiO contacts, as pure NiO exhibited significantly higher conductance. Therefore, ZnO morphological control is critical for optimizing sensing performance and enabling effective heterojunction formation, offering insights into the design of high-performance chemoresistive sensors.

CRediT authorship contribution statement

Pedro Paulo Ortega: Conceptualization, Formal analysis, Investigation, Visualization, Writing – original draft, Writing – review & editing. **Sandro Gherardi:** Data curation, Formal analysis, Writing – review & editing. **Elena Spagnoli:** Formal analysis, Writing – review & editing. **Giulia Zonta:** Writing – review & editing. **Michele Astolfi:** Formal analysis, Writing – review & editing. **Giuseppe Cruciani:** Formal analysis, Writing – review & editing. **Valmor Roberto Mastelaro:** Formal analysis, Investigation. **Miguel Adolfo Ponce:** Formal analysis, Writing – review & editing. **Cesare Malagù:** Formal analysis, Resources, Supervision, Writing – review & editing. **Elson Longo:** Formal analysis, Funding acquisition, Resources, Supervision, Writing – review & editing.

Declaration of Competing Interest

The authors declare the following financial interests/personal relationships, which may be considered as potential competing interests: Given his role as Editor of the Journal of Alloys and Compounds, Prof. Valmor Roberto Mastelaro had no involvement in the peer review of this article and had no access to information regarding its peer review. Full responsibility for the editorial process for this article was delegated to another journal editor." If there are other authors, they declare that they have no known competing financial interests or personal relationships that could have appeared to influence the work reported in this paper.

Acknowledgements

We gratefully acknowledge the financial support of the São Paulo State Research Foundation (FAPESP) to the development of this work (Grant numbers 2023/07486–8, 2024/08759–0, and 2013/07296–2). We thank SCENT S.r.l. for providing access to the necessary equipment and technical facilities used in this research. We also thank Dr. Lara Kelly Ribeiro for her assistance with the Mott-Schottky measurements.

Appendix A. Supporting information

Supplementary data associated with this article can be found in the online version at doi:10.1016/j.jallcom.2026.188279.

References

[1] M.A. Franco, P.P. Conti, R.S. Andre, D.S. Correa, A review on chemiresistive ZnO gas sensors, Sens. Actuators Rep. 4 (2022) 100100, https://doi.org/10.1016/J.SNR.2022.100100.

[2] J. Hu, H. Ma, Y. Zhou, L. Ma, S. Zhao, S. Shi, J. Li, Y. Chang, Gas-sensing properties and mechanisms of 3d networks composed of zno tetrapod micro-nano structures at room temperature, Page 203 17, Materials 2024 17 (2023) 203, https://doi.org/10.3390/MA17010203.

[3] K. Hu, Y. Cai, Z. Wang, Z. Zhang, J. Xian, C. Zhang, A review on metal oxide semiconductor-based chemo-resistive ethylene sensors for agricultural applications, Page 13 12, Chemosensors 2024 12 (2024) 13, https://doi.org/10.3390/CHEMOSENSORS12010013.

[4] G. Mineo, K. Moulaee, G. Neri, S. Mirabella, E. Bruno, H2 detection mechanism in chemoresistive sensor based on low-cost synthesized WO3 nanorods, Sens. Actuators B Chem. 348 (2021) 130704, https://doi.org/10.1016/J.SNB.2021.130704.

[5] U. Yaqoob, M.I. Younis, Chemical Gas Sensors: Recent Developments, Challenges, and the Potential of Machine Learning—A Review, Page 2877 21, Sensors 2021 21 (2021) 2877, https://doi.org/10.3390/S21082877.

[6] C.E. Simion, B. Junker, U. Weimar, A. Stanoiu, N. Bârsan, Sensing mechanisms of CO and H2 with NiO material – DRIFTS investigations, Sens. Actuators B Chem. 390 (2023) 134028, https://doi.org/10.1016/J.SNB.2023.134028.

[7] B. Saruhan, R. Lontio Fomekong, S. Nahirniak, Review: influences of semiconductor metal oxide properties on gas sensing characteristics, Front. Sens. 2 (2021) 657931, https://doi.org/10.3389/FSENS.2021.657931.

[8] I. Boehme, U. Weimar, N. Barsan, Unraveling the surface chemistry of CO Sensing with In_2O_3 based gas sensors, Sens. Actuators B Chem. 326 (2021) 129004, https://doi.org/10.1016/J.SNB.2020.129004.

[9] E. Spagnoli, B. Fabbri, A. Gaiardo, M. Valt, M. Ardit, S. Krik, G. Cruciani, M. Della Ciana, L. Vanzetti, G. Vola, F. Di Benedetto, A. Migliori, C. Malagù, V. Guidi, Design of a metal-oxide solid solution for selective detection of ethanol with marginal influence by humidity, Sens. Actuators B Chem. 370 (2022) 132426, https://doi.org/10.1016/J.SNB.2022.132426.

[10] A. Nasriddinov, T. Shatalova, S. Maksimov, X. Li, M. Rumyantseva, Humidity effect on low-temperature nh3 sensing behavior of In_2O_3/rGO Composites under UV Activation, Page 1517 23, Sensors 2023 23 (2023) 1517, https://doi.org/10.3390/S23031517.

[11] T.M. Perfecto, C.A. Zito, D.P. Volanti, Effect of NiS nanosheets on the butanone sensing performance of ZnO hollow spheres under humidity conditions, Sens. Actuators B Chem. 334 (2021) 129684, https://doi.org/10.1016/J.SNB.2021.129684.

[12] D.H. Gao, Q.C. Yu, M.A. Kebeded, Y.Y. Zhuang, S. Huang, M.Z. Jiao, X.J. He, Advances in modification of metal and noble metal nanomaterials for metal oxide gas sensors: a review, 44, Rare Met. 2025 44 (3) (2025) 1443–1496, https://doi.org/10.1007/S12598-024-03027-7.

[13] M. Zhu, H. Zhang, S. Zhang, H. Yao, X. Shi, S. Xu, Chemoresistive gas sensors based on noble-metal-decorated metal oxide semiconductors for H2 Detection, Page 451 18, Materials 2025 18 (2025) 451, https://doi.org/10.3390/MA18020451.

[14] A. Fioravanti, P. Marani, S. Morandi, S. Lettieri, M. Mazzocchi, M. Sacerdoti, M. C. Carotta, Growth Mechanisms of ZnO micro-nanomorphologies and their role in enhancing gas sensing properties, Page 1331 21, Sensors 2021 21 (2021) 1331, https://doi.org/10.3390/S21041331.

[15] P.P. Ortega, S. Gherardi, E. Spagnoli, B. Fabbri, N. Landini, C. Malagù, C. Macchi, C.M. Aldao, M.A. Ponce, A.Z. Simões, E. Longo, Deciphering the CO sensing mechanisms of CeO2-based nanostructured semiconductors: influence of doping, morphology, and humidity, Sens. Actuators B Chem. 440 (2025) 137921, https://doi.org/10.1016/J.SNB.2025.137921.

[16] S. Gbadamasi, M. Mohiuddin, V. Krishnamurthi, R. Verma, M.W. Khan, S. Pathak, K. Kalantar-Zadeh, N. Mahmood, Interface chemistry of two-dimensional heterostructures – fundamentals to applications, Chem. Soc. Rev. 50 (2021) 4684–4729, https://doi.org/10.1039/D0CS01070G.

[17] W. yu Li, H. Yu, M. Yang, X. Dong, Y. Yang, T. Wang, Gas-sensitive performances of Zn/W-PTA derivative composite excited by a single UV-LED, J. Alloy. Compd. 1050 (2026) 185691, https://doi.org/10.1016/J.JALLCOM.2025.185691.

[18] W. Li, H. Yu, M. Yang, X. Dong, Y. Yang, T. Wang, Natural sunlight excited ZnO/ZIF-8 derivative NOx gas sensor and its application in automobile exhaust gas detection, Sens. Actuators B Chem. 449 (2026) 139074, https://doi.org/10.1016/J.SNB.2025.139074.

[19] M.R. Alenezi, A.S. Alshammari, K.D.G.I. Jayawardena, M.J. Beliatis, S.J. Henley, S. R.P. Silva, Role of the exposed polar facets in the performance of thermally and UV Activated ZnO nanostructured gas sensors, J. Phys. Chem. C. Nanomater. Interfaces 117 (2013) 17850, https://doi.org/10.1021/JP4061895.

[20] S. Xu, J. Lu, D. Jin, H. Jin, SnS2 with different exposed crystal planes for NO2 gas sensing, Chem. Phys. 582 (2024) 112296, https://doi.org/10.1016/J.CHEMPHYS.2024.112296.

[21] X. Bai, Z. Li, C. Yang, J. Fang, J. Liu, Y. Zhang, D. Wang, Y. Qie, Study on gas sensitive behavior of SnO2(221) and (110) crystal planes, Vacuum 218 (2023) 112648, https://doi.org/10.1016/J.VACUUM.2023.112648.

[22] S. Yang, G. Lei, H. Xu, Z. Lan, Z. Wang, H. Gu, Metal oxide based heterojunctions for gas sensors: A review, Nanomaterials 11 (2021) 1026, https://doi.org/10.3390/NANO11041026/S1.

[23] X. Wang, X. Han, S. Xie, Q. Kuang, Y. Jiang, S. Zhang, X. Mu, G. Chen, Z. Xie, L. Zheng, Controlled synthesis and enhanced catalytic and gas-sensing properties of tin dioxide nanoparticles with exposed high-energy facets, Chem. - A Eur. J. 18 (2012) 2283–2289, https://doi.org/10.1002/CHEM.201103280.

[24] H. Liu, Z. Wang, G. Cao, G. Pan, X. Yang, M. Qiu, C. Sun, J. Shao, Z. Li, H. Zhang, Construction of hollow NiO/ZnO p-n heterostructure for ultrahigh performance toluene gas sensor, Mater. Sci. Semicond. Process 141 (2022) 106435, https://doi.org/10.1016/J.MSSP.2021.106435.

[25] P. Makuła, M. Pacia, W. Macyk, How to correctly determine the band gap energy of modified semiconductor photocatalysts based on UV-Vis Spectra, J. Phys. Chem. Lett. 9 (2018) 6814–6817, https://doi.org/10.1021/acs.jpclett.8b02892.

[26] W.L. de Almeida, L.C. Freisleben, B.C. Brambilla, V.G. Isoppo, F.S. Rodembusch, V. C. de Sousa, Influence of starch used in the sol-gel synthesis of ZnO nanopowders, J. Nanopart. Res. 25 (2023) 1–13, https://doi.org/10.1007/S11051-023-05730-5.

[27] R.B. da Silva, R.A. Pinto, J.M. Soares, A. Franco, M.A. Correa, F. Bohn, J.A.P. da Costa, Effect of the synthesis method and calcination temperature on the formation of Ni–NiO nanocomposites, J. Solgel Sci. Technol. 91 (2019) 286–294, https://doi.org/10.1007/S10971-019-05038-8.

[28] P.P. Ortega, J.V.N. Palma, A.L. Doimo, L. Líbero, G.F. Yamakawa, L.G. Merízio, E. C. Aguiar, L.F. Silva, E. Longo, Influence of different synthesis methods on the defect structure, morphology, and uv-assisted ozone sensing properties of zinc oxide nanoplates, Chemosensors 13 (2025) 152, https://doi.org/10.3390/CHEMOSENSORS13040152/S1.

[29] S.K. Lim, S. –H. Hwang, J. Jung, M.G. Jeong, Synthesis of zinc oxide nanorods and plates by solvothermal method, Phys. Chem. Appl. Nanostruct. (2017) 361–364, https://doi.org/10.1142/9789813224537_0083.

[30] S. Agarwal, L.K. Jangir, K.S. Rathore, M. Kumar, K. Awasthi, Morphology-dependent structural and optical properties of ZnO nanostructures, Appl. Phys. A Mater. Sci. Process 125 (2019) 1–7, https://doi.org/10.1007/S00339-019-2852-X.

[31] A. Al-Rasheedi, N.H. Alonizan, M.S. Aida, Effect of zinc nitrate concentration on the morphology of ZnO nanostructures grown by hydrothermal method, Physica Status Solidi (A) Applications Materials Science 220 (2023) 2200905, https://doi.org/10.1002/PSSA.202200905.

[32] A. Kubiak, S. Żółtowska, E. Gabała, M. Szybowicz, K. Siwińska-Ciesielczyk, T. Jesionowski, Controlled microwave-assisted and pH-affected growth of ZnO structures and their photocatalytic performance, Powder Technol. 386 (2021) 221–235, https://doi.org/10.1016/J.POWTEC.2021.03.051.

[33] A.C. Catto, L.F. Da Silva, C. Ribeiro, S. Bernardini, K. Aguir, E. Longo, V. R. Mastelaro, An easy method of preparing ozone gas sensors based on ZnO nanorods, RSC Adv. 5 (2015) 19528–19533, https://doi.org/10.1039/C5RA00581G.

[34] Y. Zhang, M. Muhammed, Critical evaluation of thermodynamics of complex formation of metal ions in aqueous solutions: VI. Hydrolysis and hydroxo-complexes of Zn^{2+} at 298.15 K, Hydrometallurgy 60 (2001) 215–236, https://doi.org/10.1016/S0304-386X(01)00148-7.

[35] A. Sedlak, W. Janusz, Specific adsorption of carbonate ions at the zinc oxide/electrolyte solution interface, Physicochem. Probl. Miner. Process. 42 (2008) 57–66.

[36] M.E. McMahon, R.J. Santucci, J.R. Scully, Advanced chemical stability diagrams to predict the formation of complex zinc compounds in a chloride environment, RSC Adv. 9 (2019) 19905–19916, https://doi.org/10.1039/C9RA00228F.

[37] R.A. Reichle, K.G. McCurdy, L.G. Hepler, Zinc Hydroxide: Solubility Product and Hydroxy-complex Stability Constants from 12.5 to 75 °C, Can. J. Chem. 53 (2011) 3841–3845, https://doi.org/10.1139/v75-556.

[38] S. Cho, J.W. Jang, S.H. Jung, B.R. Lee, E. Oh, K.H. Lee, Precursor effects of citric acid and citrates on ZnO crystal formation, Langmuir 25 (2009) 3825–3831, https://doi.org/10.1021/LA804009G.

[39] K. Swaroop, H.M. Somashekarappa, Effect of pH values on surface Morphology and Particle size variation in ZnO Nanoparticles Synthesised by co-precipitation Method, Res. J. Recent Sci. 4 (2015) 197–201.

[40] K. Sambath, M. Saroja, M. Venkatachalam, K. Rajendran, N. Muthukumarasamy, Morphology controlled synthesis of ZnO nanostructures by varying pH, Journal Materials Science Materials Electronics 23 (2012) 431–436, https://doi.org/10.1007/S10854-011-0507-6.

[41] A.B. Pandit, A.U. Badnore, Effect of pH on sonication assisted synthesis of ZnO nanostructures: Process details, Chem. Eng. Process. Process.Intensif. 122 (2017) 235–244, https://doi.org/10.1016/J.CEP.2017.09.013.

[42] B. Cheng, X. Wang, L. Liu, L. Guo, Growth mechanism and morphology dependent luminescence properties of ZnO nanostructures prepared in aqueous solution, Mater. Lett. 62 (2008) 3099–3102, https://doi.org/10.1016/J.MATLET.2008.01.115.

[43] A.F. Gouveia, S.C.S. Lemos, E.R. Leite, E. Longo, J. Andrés, Back to the Basics: Probing the Role of Surfaces in the Experimentally Observed Morphological Evolution of ZnO, Page 978 13, Nanomaterials 2023 13 (2023) 978, https://doi.org/10.3390/NANO13060978.

[44] X.G. Han, H.Z. He, Q. Kuang, X. Zhou, X.H. Zhang, T. Xu, Z.X. Xie, L.S. Zheng, Controlling morphologies and tuning the related properties of nano/microstructured ZnO crystallites, J. Phys. Chem. C. 113 (2009) 584–589, https://doi.org/10.1021/JP808233E.

[45] S.S. Pawar, R.S. Redekar, N.L. Tarwal, Exploring the photocatalytic activity of surfactant-free ZnO micro-flowers synthesized by microwave-assisted method, Inorg. Chem. Commun. 162 (2024) 112106, https://doi.org/10.1016/J.INOCHE.2024.112106.

[46] K. Manjunath, T.N. Ravishankar, D. Kumar, K.P. Priyanka, T. Varghese, H.R. Naika, H. Nagabhushana, S.C. Sharma, J. Dupont, T. Ramakrishnappa, G. Nagaraju, Facile combustion synthesis of ZnO nanoparticles using Cajanus cajan (L.) and its multidisciplinary applications, Mater. Res. Bull. 57 (2014) 325–334, https://doi.org/10.1016/J.MATERRESBULL.2014.06.010.

[47] J. Rosowska, J. Kaszewski, M. Krajewski, A. Małolepszy, B.S. Witkowski, Ł. Wachnicki, L.I. Bulyk, P. Sybilski, M. Godlewski, M.M. Godlewski, Growth of ZnO nanoparticles using microwave hydrothermal method—search for defect-free particles, Page 230 15, Nanomaterials 2025 15 (2025) 230, https://doi.org/10.3390/NANO15030230.

[48] S.S. Kongbrailatpam, K. Singh, N. Sharma, S. None, P. Das, D. Kumar, M. Kumar, S. Kumar, S. Ghotekar, P.E. Lokhande, S. Awasthi, Unveiling the influence of dopants on structural, defect chemistry, morphological and optical characteristics

of NiO nanostructures, Phys. Scr. 99 (2024) 125002, https://doi.org/10.1088/1402-4896/AD883F.
[49] S. Mohseni Meybodi, S.A. Hosseini, M. Rezaee, S.K. Sadrnezhaad, D. Mohammadyani, Synthesis of wide band gap nanocrystalline NiO powder via a sonochemical method, Ultrason. Sonochem. 19 (2012) 841–845, https://doi.org/10.1016/J.ULTSONCH.2011.11.017.
[50] Ramseena Thundiyil, P. Poornesh, K. Ozga, J. Jedryka, An insight in to microwave induced defects and its impact on nonlinear process in NiO nanostructures under femtosecond and continuous wave laser excitation, RSC Adv. 14 (2024) 30011–30036, https://doi.org/10.1039/D4RA06056C.
[51] A.J. Deotale, U. Singh, K. Rattawa, D. Shukla, A. Gome, Role of heat treatment on nickel oxide nanoparticles: energy band gap and their effectiveness as antibacterial agents, J. Phys. Conf. Ser. 2603 (2023) 012009, https://doi.org/10.1088/1742-6596/2603/1/012009.
[52] G. Rajender, P.K. Giri, Strain induced phase formation, microstructural evolution and bandgap narrowing in strained TiO_2 nanocrystals grown by ball milling, J. Alloy. Compd. 676 (2016) 591–600, https://doi.org/10.1016/J.JALLCOM.2016.03.154.
[53] S. Dolabella, A. Borzì, A. Dommann, A. Neels, Lattice strain and defects analysis in nanostructured semiconductor materials and devices by high-resolution x-ray diffraction: theoretical and practical aspects, Small Methods 6 (2022) 2100932, https://doi.org/10.1002/SMTD.202100932.
[54] R. Xie, Z. Guo, X. Li, H. Liu, H. Sun, B. Guo, Q. Liu, Y. Li, Rational manipulation of lattice strain to tailor the electronic and optical properties of nanostructures, Ceram. Int. 47 (2021) 31476–31484, https://doi.org/10.1016/J.CERAMINT.2021.08.025.
[55] J.M. Vohs, M.A. Barteau, Dehydration and dehydrogenation of ethanol and 1-propanol on the polar surfaces of zinc oxide, Surf. Sci. 221 (1989) 590–608.
[56] C. Wang, L. Yin, L. Zhang, D. Xiang, R. Gao, Metal oxide gas sensors: Sensitivity and influencing factors, Sensors 10 (2010) 2088–2106, https://doi.org/10.3390/s100302088.
[57] S.H. Na, C.H. Park, First-principles study of the surface energy and atom cohesion of wurtzite zno and zns - implications for nanostructure formation, J. Korean Phys. Soc. 56 (2010) 498–502, https://doi.org/10.3938/JKPS.56.498.
[58] H. Ye, G. Chen, H. Niu, Y. Zhu, L. Shao, Z. Qiao, Structures and mechanisms of water adsorption on ZnO(0001) and GaN(0001) surface, J. Phys. Chem. C. 117 (2013) 15976–15983, https://doi.org/10.1021/JP312847R.
[59] T. Morimoto, M. Nagao, Adsorption anomaly in the system zinc oxide-water, J. Phys. Chem. 78 (1974) 1116–1120, https://doi.org/10.1021/J100604A014.
[60] B. Meyer, D. Marx, O. Dulub, U. Diebold, M. Kunat, D. Langenberg, C. Wöll, Partial dissociation of water leads to stable superstructures on the surface of zinc oxide, Angew. Chem. Int. Ed. 43 (2004) 6641–6645, https://doi.org/10.1002/ANIE.200461696.
[61] M. Casarin, C. Maccato, A. Vittadini, An LCAO-LDF study of the chemisorption of H2O and H2S on ZnO(0001) and ZnO(10^{ī}0), Surf. Sci. 377–379 (1997) 587–591, https://doi.org/10.1016/S0039-6028(96)01452-5.
[62] S. Gherardi, M. Astolfi, A. Gaiardo, C. Malagù, G. Rispoli, D. Vincenzi, G. Zonta, Investigating the temperature-dependent kinetics in humidity-resilient tin–titanium-based metal oxide gas sensors, Page 151 12, Chemosensors 2024 12 (2024) 151, https://doi.org/10.3390/CHEMOSENSORS12080151.
[63] C.N. Wang, Y.L. Li, F.L. Gong, Y.H. Zhang, S.M. Fang, H.L. Zhang, Advances in Doped ZnO Nanostructures for Gas Sensor, Chem. Rec. 20 (2020) 1553–1567, https://doi.org/10.1002/TCR.202000088.
[64] N. Barsan, U. Weimar, Conduction model of metal oxide gas sensors, J. Electroceram 7 (2001) 143–167, https://doi.org/10.1023/A:1014405811371/METRICS.
[65] F. Schipani, D.R. Miller, M.A. Ponce, C.M. Aldao, S.A. Akbar, P.A. Morris, J.C. Xu, Conduction mechanisms in SnO2 single-nanowire gas sensors: an impedance spectroscopy study, Sens. Actuators B Chem. 241 (2017) 99–108, https://doi.org/10.1016/J.SNB.2016.10.061.
[66] P.P. Ortega, C.C. Silva, M.A. Ramirez, G. Biasotto, C.R. Foschini, A.Z. Simões, Multifunctional environmental applications of ZnO nanostructures synthesized by the microwave-assisted hydrothermal technique, Appl. Surf. Sci. 542 (2021) 148723, https://doi.org/10.1016/j.apsusc.2020.148723.
[67] Y. He, M. Jiao, A Mini-Review on Metal Oxide Semiconductor Gas Sensors for Carbon Monoxide Detection at Room Temperature, Page 55 12, Chemosensors 2024 12 (2024) 55, https://doi.org/10.3390/CHEMOSENSORS12040055.
[68] M.A. Franco, P.P. Conti, R.S. Andre, D.S. Correa, A review on chemiresistive ZnO gas sensors, Sens. Actuators Rep. 4 (2022) 100100, https://doi.org/10.1016/J.SNR.2022.100100.
[69] N. Hongsith, E. Wongrat, T. Kerdcharoen, S. Choopun, Sensor response formula for sensor based on ZnO nanostructures, Sens. Actuators B Chem. 144 (2010) 67–72, https://doi.org/10.1016/J.SNB.2009.10.037.
[70] C. Chen, X. Zhu, H. Yu, M. Yang, X. Dong, Y. Yang, Preparation of dendritic ZnO/Ag-QDs/AgCl photocatalysts and its photodegradation of organic dyes and antibiotics, Solid State Sci. 168 (2025) 108025, https://doi.org/10.1016/J.SOLIDSTATESCIENCES.2025.108025.
[71] V. Perumal, U. Hashim, S.C.B. Gopinath, H.R. Prasad, L. Wei-Wen, S. R. Balakrishnan, T. Vijayakumar, R.A. Rahim, Characterization of gold-sputtered zinc oxide nanorods—a potential hybrid material, 1 11, Nanoscale Res. Lett. 2016 11 (2016) 31, https://doi.org/10.1186/S11671-016-1245-8.
[72] A.N. Mansour, Characterization of NiO by XPS, Surf. Sci. Spectra 3 (1994) 231–238, https://doi.org/10.1116/1.1247751.
[73] V. Manjunath, S. Bimli, D. Singh, R. Biswas, P.N. Didwal, K.K. Haldar, N. G. Deshpande, P.A. Bhobe, R.S. Devan, Porous nanorods by stacked NiO nanoparticulate exhibiting corn-like structure for sustainable environmental and energy applications, RSC Adv. 13 (2023) 21962–21970, https://doi.org/10.1039/D3RA03209D.
[74] C. Liu, B. Wang, T. Liu, P. Sun, Y. Gao, F. Liu, G. Lu, Facile synthesis and gas sensing properties of the flower-like NiO-decorated ZnO microstructures, Sens. Actuators B Chem. 235 (2016) 294–301, https://doi.org/10.1016/J.SNB.2016.05.064.
[75] H. Liu, Q. Zhou, Q. Zhang, C. Hong, L. Xu, L. Jin, W. Chen, Synthesis, characterization and enhanced sensing properties of a NiO/ZnO p–n Junctions Sensor for the SF6 decomposition byproducts SO2, SO2F2, and SOF2, 913 17, Sensors 2017 17 (2017) 913, https://doi.org/10.3390/S17040913.
[76] M.H. Raza, N. Kaur, E. Comini, N. Pinna, Toward optimized radial modulation of the space-charge region in one-dimensional SnO2-NiO core-shell nanowires for hydrogen sensing, ACS Appl. Mater. Interfaces 12 (2020) 4594–4606, https://doi.org/10.1021/ACSAMI.9B19442.
[77] M.H. Huang, M. Madasu, Facet-dependent and interfacial plane-related photocatalytic behaviors of semiconductor nanocrystals and heterostructures, Nano Today 28 (2019) 100768, https://doi.org/10.1016/J.NANTOD.2019.100768.
[78] C. Ai, B. Wang, K. Duan, J. Jiang, Z. Jiang, S. Hu, B. Luo, L. Ma, D. Jing, Enhanced photocatalytic activity by regulating charge transferring: Unveiling the decisive role of cerium oxide crystal-facet engineering over heterojunction, J. Colloid Interface Sci. 636 (2023) 341–350, https://doi.org/10.1016/J.JCIS.2022.12.139.
[79] Z. Zhao, H. Yang, Z. Wei, Y. Xue, Y. Sun, W. Zhang, P. Li, W. Gong, S. Zhuiykov, J. Hu, NH3 Sensor based on 3d hierarchical flower-shaped n-ZnO/p-NiO heterostructures yields outstanding sensing capabilities at ppb Level, Page 4754 20, Sensors 2020 20 (2020) 4754, https://doi.org/10.3390/S20174754.
[80] Y. Lu, Y. Ma, S. Ma, S. Yan, Hierarchical heterostructure of porous NiO nanosheets on flower-like ZnO assembled by hexagonal nanorods for high-performance gas sensor, Ceram. Int. 43 (2017) 7508–7515, https://doi.org/10.1016/J.CERAMINT.2017.03.032.
[81] L. Liu, Y. Zhang, G. Wang, S. Li, L. Wang, Y. Han, X. Jiang, A. Wei, High toluene sensing properties of NiO–SnO2 composite nanofiber sensors operating at 330 °C, Sens. Actuators B Chem. 160 (2011) 448–454, https://doi.org/10.1016/J.SNB.2011.08.007.